

# DISSECTING THE PROPERTIES OF OPTICALLY-THICK HYDROGEN AT THE PEAK OF COSMIC STAR FORMATION HISTORY

MICHELE FUMAGALLI<sup>1,2,6</sup>, JOHN M. O'MEARA<sup>3</sup>, J. XAVIER PROCHASKA<sup>4</sup>, AND GABOR WORSECK<sup>5</sup>

*Draft version November 30, 2018*

## ABSTRACT

We present results of a blind survey of Lyman limit systems (LLSs) detected in absorption against 105 quasars at  $z \sim 3$  using the blue sensitive MagE spectrograph at the Magellan Clay telescope. By searching for Lyman limit absorption in the wavelength range  $\lambda \sim 3000 - 4000 \text{ \AA}$ , we measure the number of LLSs per unit redshift  $\ell(z) = 1.21 \pm 0.28$  at  $z \sim 2.8$ . Using a stacking analysis, we further estimate the mean free path of ionizing photons in the  $z \sim 3$  Universe  $\lambda_{\text{mfp}}^{912} = 100 \pm 29 \text{ h}_{70.4}^{-1} \text{ Mpc}$ . Combined with our LLS survey, we conclude that systems with  $\log N_{\text{HI}} \geq 17.5 \text{ cm}^{-2}$  contribute only  $\sim 40\%$  to the observed mean free path at these redshifts. Further, with the aid of photo-ionization modeling, we infer that a population of ionized and metal poor systems is likely required to reproduce the metal line strengths observed in a composite spectrum of 20 LLSs with  $\log N_{\text{HI}} \sim 17.5 - 19 \text{ cm}^{-2}$  at  $z \sim 2.6 - 3.0$ . Finally, with a simple toy model, we deduce that gas in the halos of galaxies can alone account for the totality of LLSs at  $z \lesssim 3$ , but a progressively higher contribution from the intergalactic medium is required beyond  $z \sim 3.5$ . We also show how the weakly evolving number of LLSs per unit redshift at  $z \lesssim 3$  can be modeled either by requiring that the spatial extent of the circumgalactic medium is redshift invariant in the last  $\sim 10$  Gyr of cosmic evolution or by postulating that LLSs arise in halos that are rare fluctuations in the density field at each redshift.

*Subject headings:* quasars: absorption lines — cosmology: observations — intergalactic medium — galaxies: high-redshift — galaxies: halos

## 1. INTRODUCTION

The redshift distribution of the denser hydrogen clouds in the Universe is a relevant quantity for several cosmological studies, such as characterizing the UV extragalactic background radiation (e.g. Madau et al. 1999; Faucher-Giguère et al. 2009; Haardt & Madau 2012) or establishing the cosmic metal budget (e.g. Prochaska et al. 2006; Bouché et al. 2007). Empirically, these clouds can be easily identified as Lyman limit systems (LLSs) in spectra of background quasars (Tytler 1982). By definition, these gas pockets have sufficient column density of neutral hydrogen ( $N_{\text{HI}} \geq 10^{17.2} \text{ cm}^{-2}$ ) to become optically thick at the Lyman continuum ( $< 912 \text{ \AA}$ ) such that they imprint a characteristic spectral signature on the underlying continuum of background quasars.

Since the first discoveries of LLSs, a series of seminal surveys (Tytler 1982; Sargent et al. 1989) have attempted to quantify  $\ell(z)$ , the redshift evolution of the number per unit redshift of these absorbers. In the past two decades, several efforts have been undertaken

to expand the sample size of known LLSs and to better constrain  $\ell(z)$  across an increasingly large redshift interval (e.g. Lanzetta 1991; Storrie-Lombardi et al. 1994; Stengler-Larrea et al. 1995; Songaila & Cowie 2010). However, these searches have yielded contrasting results, leaving substantial uncertainties on the actual redshift evolution of optically-thick hydrogen clouds (see figure 16 of Prochaska et al. 2010). Possible reasons for this disagreement are inconsistent definitions for the minimum column density at which LLSs are defined or, for some studies, the fact that LLSs are compiled from the literature, resulting in heterogeneous quasar samples. To overcome some of these limitations, new surveys or archival studies (Prochaska et al. 2010; Ribaudo et al. 2011a; O'Meara et al. 2013) have focused in recent years on statistical samples of quasars in narrow redshift intervals. Further, these data have been analyzed with attention to possible selection biases and with the goal of selecting only LLSs above a well-defined column density limit. As a result,  $\ell(z)$  is now more accurately constrained between  $z \sim 0.5 - 4.5$  for systems with  $N_{\text{HI}} \geq 10^{17.5} \text{ cm}^{-2}$ , the column density at which the optical depth at the Lyman limit exceeds  $\tau \geq 2$ . These studies have also provided us with a refined determination of another relevant cosmological quantity, the mean free path of ionizing photons  $\lambda_{\text{mfp}}^{912}$ , that is now well measured between  $z \sim 2 - 5$  (Prochaska et al. 2009; O'Meara et al. 2013; Worseck et al. in prep.).

Unfortunately, the difficulties of collecting large spectroscopic samples of quasars with coverage of the bluest wavelengths accessible from the ground ( $\lambda \sim 3200 - 4000 \text{ \AA}$ ) have hampered a revised determination of  $\ell(z)$  and  $\lambda_{\text{mfp}}^{912}$  between  $z \sim 2.5 - 3.5$ . Occurring at one of

This paper includes data gathered with the 6.5 meter Magellan Telescopes located at Las Campanas Observatory, Chile and with the 3-m Shane Telescope at Lick Observatory.

<sup>1</sup> Carnegie Observatories, 813 Santa Barbara Street, Pasadena, CA 91101, USA. mfumagalli@obs.carnegiescience.edu

<sup>2</sup> Department of Astrophysics, Princeton University, Princeton, NJ 08544-1001, USA.

<sup>3</sup> Department of Chemistry and Physics, Saint Michael's College, Colchester, VT, USA.

<sup>4</sup> University of California Observatories-Lick Observatory, University of California, Santa Cruz, CA, USA.

<sup>5</sup> Max Planck Institute for Astronomy, Königstuhl 17, D-69117, Heidelberg, Germany.

<sup>6</sup> Hubble Fellow

the most active epochs of galaxy evolution, this gap represents a limitation in our understanding of the cosmic evolution of optically-thick hydrogen clouds, mainly because of the postulated connection between LLSs and the population of star-forming galaxies (see Section 7). To help complete our modern view of the cosmic evolution of LLSs, in this paper we present results from a spectroscopic survey of 105 quasars at  $z \sim 3.0 \pm 0.2$ , conducted with the blue sensitive MagE echellette spectrograph at the Magellan telescope. This survey was specifically designed to probe the properties of LLSs at  $2.6 \lesssim z \lesssim 3$ , offering an independent determination of  $\ell(z)$  from previous surveys at similar redshifts (Sargent et al. 1989; Lanzetta 1991). Further, the higher spectral resolution allows us to identify, in addition to the Lyman break, part of the Lyman series as well as the associated metal lines that can be used to gain insight into the physical properties of LLSs (e.g. Prochaska 1999).

The outline of this paper is the following. A description of the observations and data reduction is provided in Section 2. In Section 3 and Section 4, we present the MagE quasar composite spectrum at  $z \sim 3$  together with the measurement of the mean free path of ionizing photons in the  $z \sim 3$  Universe. The search of LLSs and the new determination of  $\ell(z)$  at  $z \sim 2.8$  is presented in Section 5, while Section 6 focuses on the chemical and ionization properties of the composite spectrum of a statistical sample of LLSs. Finally, a simple toy model to describe the connection between LLSs and galaxies is offered in Section 7, while a summary concludes this paper in Section 8. Throughout this work, we assume a  $\Lambda$ CDM cosmology described by  $\Omega_\Lambda = 0.728$ ,  $\Omega_m = 0.272$ , and  $H_0 = 70.4 \text{ km s}^{-1} \text{ Mpc}^{-1}$  (Komatsu et al. 2011).

## 2. OBSERVATIONS AND DATA REDUCTION

With the aim of constraining  $\ell(z)$  and  $\lambda_{\text{mfp}}^{912}$  between  $2.6 \lesssim z \lesssim 3.0$ , we have observed 105 quasars at  $z_{\text{qso}} \sim 3.0 \pm 0.2$  using the MagE echellette spectrograph ( $R \sim 4100$ ) at the Magellan Clay telescope (Marshall et al. 2008). The high throughput of MagE down to  $\lambda \sim 3100 \text{ \AA}$  ensures optimal coverage of the Lyman limit across the redshift range  $z \sim 2.6 - 3.0$ . The targeted quasars have been selected without any prior knowledge on the presence of absorbers along the line of sight. Only half of our sample (hereafter referred to as the color selected sample) has been drawn from the quasar spectroscopic catalogue of the Sloan Digital Sky Survey (SDSS; Schneider et al. 2010), while the remaining half of the targets (non-color selected) have been compiled from the literature to include only quasars that were first discovered either with radio or X-ray observations, or through slitless spectroscopy or optical variability. These two different samples have been assembled to further explore and avoid a potential bias against sightlines free of strong intervening absorbers that has been recently discovered in the optical color selection algorithm adopted by SDSS (Worseck & Prochaska 2011).

Observations have been conducted between the year 2009 and the year 2012, as detailed in Table 1, for the most part under clear skies. The simple optical design of MagE and our consistent choice of the  $0.7''$  slit have ensured a high level of homogeneity in the sample, although observations have been collected across a four year period. For each quasar, the slit was aligned with the par-

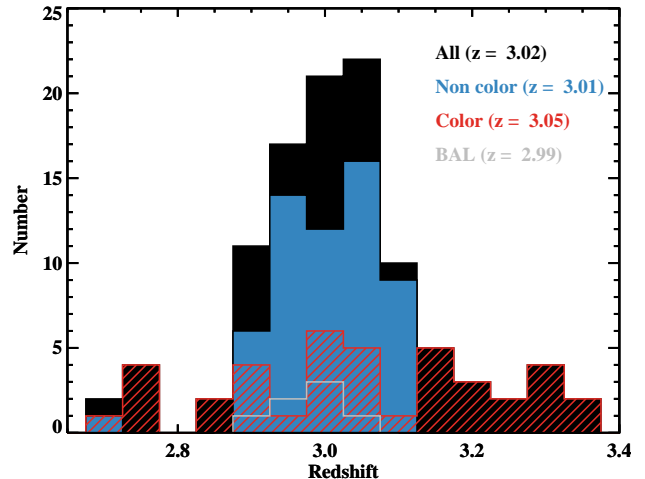


**Figure 1.** Redshift distribution for the full quasar sample (black), and for the color and non-color selected samples (red and blue, respectively). The redshifts of broad absorption line quasars are highlighted in grey. The median of these distributions are also listed. Our survey is probing a narrow redshift range centered at  $z_{\text{qso}} \sim 3$ , ideal to study the properties of optically thick gas between  $z \sim 2.6 - 3.0$ .

alactic angle to minimize the effects of atmospheric differential refraction. Throughout this survey, exposure times have been adjusted according to the quasar magnitudes and optimal scheduling of the observations. The final spectra have signal-to-noise ratios (S/N) ranging from  $\sim 10 - 50$  per  $0.4 \text{ \AA}$  pixel as measured in a  $100 \text{ \AA}$  window centered at  $5500 \text{ \AA}$ . However, because of the different sensitivity and different dispersion across orders, the listed S/N provide only a simple description of the data quality.

Data are reduced with the MASE pipeline (Bochanski et al. 2009) which, after bias subtraction and flat-fielding, extracts and combines the spectra in each order, producing a wavelength-calibrated spectrum in one dimension. Absolute flux calibration is obtained with multiple spectro-photometric stars (Feige 110, GD108, and GD50) that have been observed in between science exposures. Due to imperfect photometric conditions and slit losses, the absolute flux calibration of the science exposures is uncertain. However, this error does not affect our analysis which relies only on the relative flux calibration as a function of wavelength. A comparison of the fluxed spectro-photometric stars against template spectra reveals that the relative flux calibration of MagE data is accurate to within few percent between  $\lambda \sim 3190 - 9000 \text{ \AA}$ . And in fact, when we compare colors derived from the MagE spectra for which SDSS photometry is available, we find excellent agreement for the  $g - r$ ,  $r - i$ ,  $g - i$  colors (within  $\sim \pm 0.03 - 0.05 \text{ mag}$ ).

Not surprisingly, a larger discrepancy ( $\sim 0.3 \text{ mag}$ ) is found for the  $u - g$  color, but we exclude the presence of appreciable systematic errors in two ways. First, we flux calibrate multiple spectro-photometric stars collected during each observing night using the same sensitivity function that is applied to the science exposures. By comparing these fluxed spectra to the corresponding templates, we find agreement to within  $\sim 0.1 \text{ mag}$

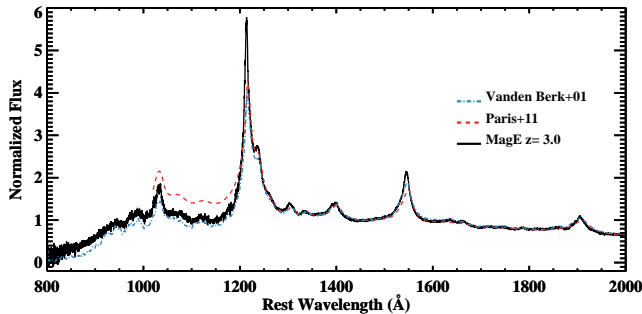


**Figure 2.** Quasar composite spectrum of 98 MagE spectra at  $z_{\text{qso}} \sim 3.0 \pm 0.2$  (black solid line). Also shown, the  $z \sim 3$  composite spectrum from Pâris et al. (2011) (red dashed line) and the composite spectrum by Vanden Berk et al. (2001) (blue dotted line). There is excellent agreement in the continuum redward to Lyman- $\alpha$ , while differences among the three templates are visible in the emission line properties. The discrepancies at  $\lambda_r < 1215$  Å arise instead from a different treatment of the IGM absorption, and from the different redshift distribution in the quasar samples.

for the  $u - g$  colors. Second, we compare MagE spectra with independent measurements made for 11 quasars<sup>7</sup> at the Shane/Lick 3 m telescope. During the nights February, 14-18 2013, we used the KAST spectrograph with the 600/7500 grating, the 600/4310 grism, the D55 dichroic, and the 2'' slit under mostly clear skies. Data have been reduced following standard procedures<sup>8</sup> and flux calibrated using repeated observations of spectrophotometric standard stars. Comparisons of these independent measurements reveal an excellent agreement in the flux calibrated spectra down to 3200Å. We therefore conclude that our relative photometric calibration is accurate to within  $\sim 10 - 15\%$  at all wavelengths of interest to this study.

During our analysis, we apply a Galactic dust-extinction correction, assuming a Milky Way extinction curve normalized to the color excess from the dust map of Schlegel et al. (1998). We also visually inspect each spectrum to identify quasars that exhibit evident broad absorption lines. Seven systems are found, and these are excluded from the quasar composite spectrum (Section 3) and the study of the mean free path (Section 4). Finally, we measure quasar redshifts ( $z_{\text{qso}}$ ) by fitting multiple Gaussian components to the Si IV, C IV, and [C III] broad emission lines. The resulting redshifts are listed in Table 1 and are shown in Figure 1. The quoted errors and associated velocities reflect only the statistical errors and do not account for possible systematic discrepancies between the broad emission lines in the rest-frame UV and the rest-frame optical narrow emission lines. A comparison between our redshift determinations and the values listed in the SDSS-DR9 quasar spectroscopic catalogue (Pâris et al. 2012) reveals good agreement, with a small median offset of  $160 \text{ km s}^{-1}$  which is within the measurement errors.

### 3. QUASAR COMPOSITE SPECTRUM

Leveraging the high S/N and moderate resolution of these spectra, we construct a quasar template in a nar-

<sup>7</sup> The quasars observed at Lick are: HE0940-1050, SDSSJ0304-0008, SDSSJ0915+0549, SDSSJ0942+0422, SDSSJ0947+1421, SDSSJ1019+0825, SDSSJ1025+0452, LBQS1209+1524, LBQS1223+1753, Q1406+123, and TXS1033+137.

<sup>8</sup> [www.icolick.org/~xavier/LowRedux/](http://www.icolick.org/~xavier/LowRedux/)

row redshift range ( $\Delta z \sim 0.2$ ) centered around  $z_{\text{qso}} \sim 3$ . Despite our small sample size, the UV sensitivity of the MagE spectrograph allows us to extend available composite spectra at similar redshifts (e.g. Pâris et al. 2011) down to  $\sim 800$ Å in the quasar rest frame, without resorting to the inclusion of higher redshift objects as, for instance, in the Vanden Berk et al. (2001) template.

The final stack is produced by averaging the flux in the quasar spectra in their rest frame, after normalizing each spectrum by the continuum value as measured in a  $10$  Å window centered at  $1400$  Å. The resulting composite spectrum is shown in Figure 2, together with the template by Pâris et al. (2011) and Vanden Berk et al. (2001). Excellent agreement is found in the continuum redward to Lyman- $\alpha$ , although each of the three templates exhibits different emission line properties. This discrepancy is expected due to variations in the quasar and host galaxy properties (e.g. metallicity, luminosity, redshift) in the three samples, especially given that the MagE composite is subject to a larger sample variance than the templates by Pâris et al. (2011) and Vanden Berk et al. (2001). For  $\lambda < 1200$ Å, instead, there are noticeable differences related to how the absorption from the intergalactic medium (IGM) has been treated. Pâris et al. (2011) correct their composite spectrum for the blanketing due to intervening Lyman- $\alpha$  forest clouds. Incidentally, we note that the ratio of the fluxes in the Pâris et al. (2011) template and in the MagE spectrum between  $1025 - 1215$ Å is fully consistent with the expected IGM absorption as recently measured by Becker et al. (2013). Conversely, the flux level in the composite spectrum by Vanden Berk et al. (2001) is  $\sim 20\%$  lower compared to our template. We ascribe this difference to the inclusion of  $z > 3.5$  quasars combined with the rapid redshift evolution of the IGM transmission that changes by  $\sim 25\%$  between  $z \sim 3$  and  $z \sim 3.5$  (Becker et al. 2013).

### 4. THE MEAN FREE PATH OF IONIZING RADIATION

Because of the intervening IGM, the quasar composite spectrum at  $\lambda < 1215$ Å differs from a simple power-law extrapolation of the flux redward to the Lyman- $\alpha$  emission line (Figure 2). In particular, the nearly exponential flux decrement seen at  $< 912$ Å contains information on the effective Lyman limit optical depth ( $\tau_{\text{eff}}^{\text{LL}}$ ) which is related to the mean free path of ionizing photons ( $\lambda_{\text{mfp}}^{912}$ ). By modeling the observed composite spectrum, it is therefore possible to extract information on the opacity that Lyman continuum photons experience, without the need of specifying the explicit form of the column density distribution function of the intervening absorbers.

In this section, we start by reviewing the adopted formalism that was first introduced by Prochaska et al. (2009) and refined by O’Meara et al. (2013), highlighting the elements that are most relevant to the present analysis. Next, we apply this methodology to the MagE composite spectrum and derive  $\lambda_{\text{mfp}}^{912}$  at  $z \sim 3$ .

#### 4.1. Formalism

We start by decomposing the observed quasar flux into three components,

$$F_{\text{obs}}(\lambda) = A\lambda^{-\alpha}q(\lambda)\exp(-\tau_{\text{eff}}) \quad (1)$$

where the power law  $A\lambda^{-\alpha}$  accounts for a large-scale continuum,  $q(\lambda)$  describes additional small-scale variations in the quasar spectral energy distribution, and  $\tau_{\text{eff}}$  models the wavelength-dependent effective optical depth arising from intervening absorbers. This last term includes the contribution of absorption both in the hydrogen Lyman series ( $\tau_{\text{eff}}^{\text{Ly}}$ ) and, at  $\lambda < 912\text{\AA}$ , in the Lyman continuum ( $\tau_{\text{eff}}^{\text{LL}}$ )

$$F_{\text{obs}}(\lambda) \sim A\lambda^{-\alpha}\bar{q}\exp(-\tau_{\text{eff}}^{\text{LL}} - \tau_{\text{eff}}^{\text{Ly}}). \quad (2)$$

In this equation, we further assume that the intrinsic quasar spectral energy distribution  $q(\lambda)$  does not evolve as a function of wavelength over the narrow range of interest to our study ( $\sim 850 - 912\text{\AA}$ ). Throughout this analysis, we further neglect additional opacity due to the presence of metal lines, which produces only a very modest variation in the flux ( $\sim 3\%$ ; Becker et al. 2013), well within the uncertainties of our measurement. To model the power-law continuum, we fit individual spectra in regions free from emission lines, between  $1430 - 1500\text{\AA}$ ,  $1600 - 1830\text{\AA}$ , and  $2000 - 2500\text{\AA}$ . The distribution of spectral indexes ( $\alpha$ ) agrees very well with the observed distribution in large samples of  $z_{\text{qso}} \sim 3$  quasars (e.g. Pâris et al. 2011) with a median  $\alpha = -1.36$ .

Next, to avoid the use of an explicit form for  $\tau_{\text{eff}}^{\text{Ly}}$  across the entire wavelength range, we model the continuum normalized spectrum ( $\tilde{F}_{\text{obs}}$ ) relative to the observed value at the Lyman limit  $\lambda_{912} = 911.76\text{\AA}$

$$f_{\text{obs}} = \frac{\tilde{F}_{\text{obs}}(\lambda < \lambda_{912})}{\tilde{F}_{\text{obs}}(\lambda_{912})} = \frac{\exp(-\tau_{\text{eff}}^{\text{LL}} - \tau_{\text{eff}}^{\text{Ly}})}{\exp(-\tau_{\text{eff}}^{\text{Ly}}(\lambda_{912}))} \quad (3)$$

In this equation, we only need to provide the redshift evolution for  $\tau_{\text{eff}}^{\text{Ly}}$ , which in previous studies (e.g. O’Meara et al. 2013) has been described by a power law of index  $\gamma_{\tau}$

$$\frac{\tau_{\text{eff}}^{\text{Ly}}(\lambda)}{\tau_{\text{eff}}^{\text{Ly}}(\lambda_{912})} = \left(\frac{1+z_{912}}{1+z_{\text{qso}}}\right)^{\gamma_{\tau}} \quad (4)$$

Here,  $z_{912}$  is the redshift at which a photon of wavelength  $\lambda$  that is emitted at  $z_{\text{qso}}$  will be absorbed at the Lyman limit

$$z_{912} = \lambda(1+z_{\text{qso}})/\lambda_{912} - 1. \quad (5)$$

In principle, one could fit for the free parameters in Equation (4), but, in practice, we find that data between  $830 - 912\text{\AA}$  do not constrain  $\gamma_{\tau}$  and  $\tau_{\text{eff}}^{\text{Ly}}(\lambda_{912})$  independently. To account for this minor ( $\sim 10 - 15\%$ ) but systematic effect, we evaluate  $\tau_{\text{eff}}^{\text{Ly}}$  numerically as

$$\tau_{\text{eff}}^{\text{Ly}}(z) = \sum_{n=1}^{\infty} \int \int_z^{z_{\text{qso}}} f(N_{\text{HI}}, z', b) \times \exp(-\tau_{\nu}^n) dN_{\text{HI}} dz' db, \quad (6)$$

where  $\tau_{\nu}$  is the line optical depth for the  $n$ -th transition in the Lyman series, and  $f(N_{\text{HI}}, z)$  is the column

density distribution function from O’Meara et al. (2013) extrapolated to  $z = 3$ . The validity of this extrapolation is supported by results presented in Section 5.

Once we have corrected the observed flux for the contribution of the Lyman series ( $\tilde{f}_{\text{obs}}$ ), we only need to model the optical depth at the Lyman limit

$$\ln \tilde{f}_{\text{obs}} = -\tau_{\text{eff}}^{\text{LL}}, \quad (7)$$

which is related to the opacity  $\kappa^{\text{LL}}(r, \nu)$  seen at each redshift by ionizing photons that have been emitted at a frequency  $\nu > \nu_{912}$ , integrated over the proper pathlength  $r$  from redshift  $z$  to  $z_{\text{qso}}$

$$\tau_{\text{eff}}^{\text{LL}}(r, \nu) = \int_0^r \kappa^{\text{LL}}(r', \nu) dr'. \quad (8)$$

In this equation, the integrand can be rewritten as the product of the redshift-dependent opacity  $\tilde{\kappa}_{912}(z)$  and the photo-ionization cross section  $\sigma_{\text{ph}} \propto \nu^{-2.75}$  which, in redshift space, becomes

$$\kappa^{\text{LL}}(z) = \tilde{\kappa}_{912}(z) \left(\frac{1+z}{1+z_{912}}\right)^{-2.75}. \quad (9)$$

For the adopted cosmology,

$$\frac{dr}{dz} = \frac{c/H_0}{(1+z)\sqrt{\Omega_{\text{m}}(1+z)^3 + \Omega_{\Lambda}}}, \quad (10)$$

where  $\Omega_{\Lambda}$  can be neglected between  $2.7 < z < 3.2$  with an error of  $\lesssim 3\%$ . As previously done in the literature (O’Meara et al. 2013), we can express the evolution of  $\tilde{\kappa}_{912}(z)$  with the following functional form

$$\tilde{\kappa}_{912}(z) = \tilde{\kappa}_{912}(z_{\text{qso}}) \left(\frac{1+z}{1+z_{\text{qso}}}\right)^{\gamma_{\text{k}}}, \quad (11)$$

but, again, we find that in practice data do not constrain  $\gamma_{\text{k}}$ . However, because  $\tilde{\kappa}_{912}(z)$  is only weakly dependent on redshift ( $\gamma_{\text{k}} \sim 0.4$  at  $z \sim 2$ ; O’Meara et al. 2013), we set  $\gamma_{\text{k}} = 0$  for the remainder of this analysis.

In the end, the final model for the normalized flux corrected for absorption in the Lyman series becomes

$$\ln \tilde{f}_{\text{obs}} = -\tau_{\text{eff}}^{\text{LL}} = \frac{c \tilde{\kappa}_{912}(z_{\text{qso}})(1+z_{912})^{2.75}}{\sqrt{\Omega_{\text{m}}}H_0} \times \frac{(1+z_{\text{qso}})^{-4.25} - (1+z_{912})^{-4.25}}{4.25}, \quad (12)$$

with  $\tilde{\kappa}_{912}(z_{\text{qso}})$  a free parameter. Finally, we define the mean free path  $\lambda_{\text{mfp}}^{912}$  as the distance between  $z_{\text{qso}}$  and  $z_{912}$  at which  $\tau_{\text{eff}}^{\text{LL}} = 1$ .

## 4.2. Results

We apply the formalism described in the previous subsection to the MagE composite spectra of both the color and non-color selected quasar samples. To find the best  $\tilde{\kappa}_{912}(z_{\text{qso}})$  that describes the observed flux we adopt a minimum  $\chi^2$  analysis in the wavelength range  $830 - 905\text{\AA}$ . The upper bound of this interval is chosen to avoid the quasar proximity region at  $> 905\text{\AA}$ , while the lower bound is set to avoid noisy data ( $S/N \lesssim 3$  per pixel). Although we are selecting an optimal wavelength region, we have verified that the best fit value for  $\lambda_{\text{mfp}}^{912}$  is largely

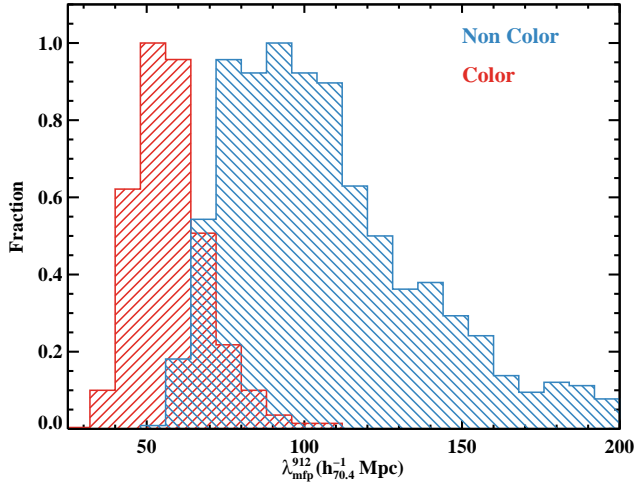


**Figure 3.** Distribution of the best fit values for  $\lambda_{\text{mfp}}^{912}$  in 1000 realizations of the quasar composite spectrum, allowing for repetitions. Both results from the color (red) and non-color (blue) selected samples are shown. Because of a selection bias that systematically avoids blue quasars, the mean free path inferred for the color selected sample is systematically lower than what is measured in the composite of non-color selected quasars.

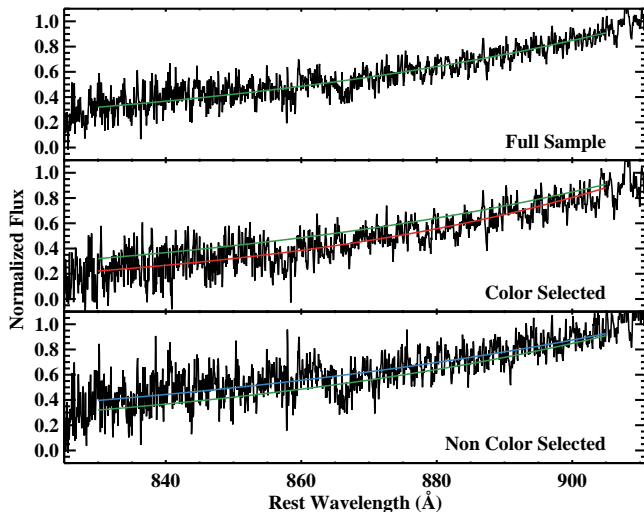


**Figure 4.** Zoom-in of the quasar composite spectra normalized at  $912\text{\AA}$  for the full sample (top, 98 quasars) and for the color (middle, 40 quasars) and non-color (bottom, 58 quasars) selected sample. The best fit models for the transmitted Lyman continuum flux (shown in green, red, and blue respectively) are superposed to emphasize the lower transmitted flux in color selected quasars compared to non-color selected ones.

insensitive to our exact choice of the spectral range included in the analysis.

Errors on  $\lambda_{\text{mfp}}^{912}$  are derived via bootstrapping by modeling 1000 composite spectra from the color and non-color selected samples which we construct as described in Section 3, but allowing for repetitions. Each composite spectrum is then normalized to the observed value at  $912 \pm 0.2 \text{\AA}$ , after introducing a random variation up to  $\pm 10\%$  in the normalization constant to account for additional uncertainties in the flux calibration. The two distributions of the best fit values for  $\lambda_{\text{mfp}}^{912}$  are shown in Figure 3.

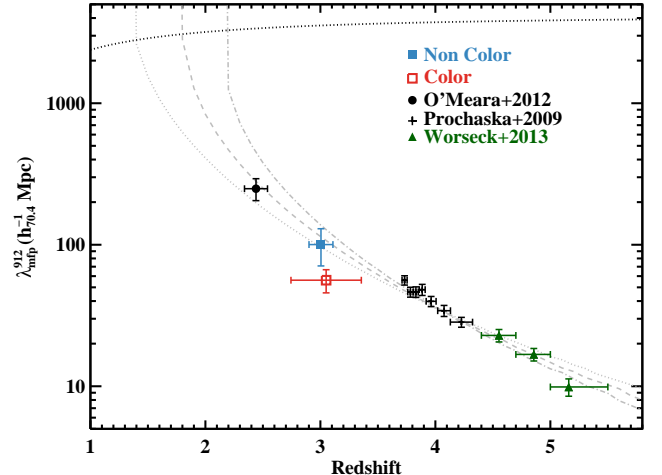


**Figure 5.** The redshift evolution of the mean free path of ionizing photons. Values measured in the color and non-color selected samples at  $z \sim 3$  are shown with open red and filled blue squares, respectively. Measurements at higher and lower redshifts from the literature are also shown (Prochaska et al. 2009; O’Meara et al. 2013; Worseck et al. in prep.). The horizon at which ionizing photons freely propagate in the Universe is marked by a black dotted line. Grey lines mark instead the analytic value of  $\lambda_{\text{mfp}}^{912}$  derived using the  $f(N_{\text{HI}}, X)$  from O’Meara et al. (2013). The normalization of the column density distribution function is modeled as a power law of index  $\gamma = 2.5, 2, 1.5$  from top to bottom. Observations favor a smooth redshift evolution with index  $\gamma \sim 2 - 1.5$ , such that ionizing photons can freely propagate in the Universe by  $z \sim 1.4 - 1.8$ .

There is a significant difference in the distributions of  $\lambda_{\text{mfp}}^{912}$  measured in color and non-color selected quasars. A Kolmogorov-Smirnov (KS) test for the color and non-color selected samples returns a KS statistic  $D = 0.81$ , and the associated probability that the two distributions in Figure 3 are drawn from the same parent population is  $\ll 10^{-5}$ . This systematic discrepancy is not only evident from the two distributions of  $\lambda_{\text{mfp}}^{912}$ , but it is also noticeable when inspecting the observed flux at  $< 912\text{\AA}$  in the composite spectra (Figure 4).

The different mean free path originates from the SDSS color selection algorithm that systematically misses blue quasars, a bias that has been previously discussed in Prochaska et al. (2009) and Worseck & Prochaska (2011). Worseck & Prochaska (2011) used mock quasar photometry to show that the SDSS color selection avoids quasars with  $u - g \lesssim 2$  between  $3 \lesssim z \lesssim 3.6$ . They also concluded that, because the presence of a LLS along the line of sight “reddens” the quasar photometry shifting its color far from the stellar locus, SDSS preferentially selects quasars with intervening absorbers. Our study of the mean free path in samples of color and non-color selected quasars, together with the survey of LLSs in the next section, confirms the presence of this bias. For this reason, in the remainder of this paper we focus our statistical analysis on the non-color selected samples, providing results from the color selected sample for comparison only.

Figure 3 also reveals that both distributions of  $\lambda_{\text{mfp}}^{912}$  exhibit a tail towards high values of  $\lambda_{\text{mfp}}^{912}$ . We interpret this feature, visible in other studies (e.g. O’Meara et al. 2013), as a consequence of sample variance in a set of quasars with a discrete number of intervening LLSs. As

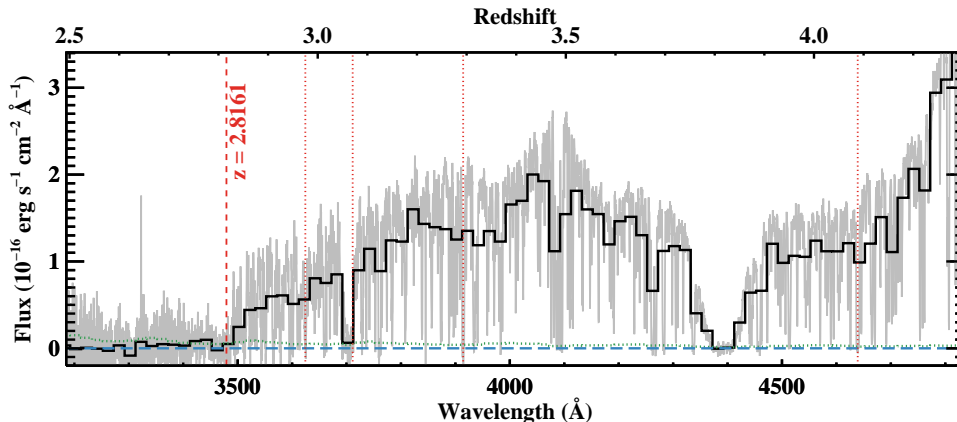


**Figure 6.2.** Blue portion of the MagE spectrum of the quasar Q0038-4041. Data at full resolution are shown in grey. The spectrum in bins of  $20\text{\AA}$  is shown in black and the green dotted line represents the associated error array. The horizontal blue line marks the zero-flux level, while the red vertical lines mark the Lyman limit (dashed line) and the first four transitions of the Lyman series (dotted lines) of the intervening LLS. The top axis translates wavelength in redshift at  $\lambda = 911.76\text{\AA}$ . Similar figures for all the quasars are available in the electronic edition of the journal (Figures 6.1-6.105).

previously done in the literature, we express our best determination of the mean free path in the  $z \sim 3$  Universe using the median value of these distributions, together with the standard deviation computed after excluding significant outliers in the tail. The mean free path from both the color and non-color selected samples are  $\lambda_{\text{mfp}}^{912} = 56 \pm 10 h_{70.4}^{-1} \text{ Mpc}$  and  $\lambda_{\text{mfp}}^{912} = 100 \pm 29 h_{70.4}^{-1} \text{ Mpc}$ . The 5th, 25th, 75th, and 95th percentiles of the distribution of  $\lambda_{\text{mfp}}^{912}$  for the non-color selected sample are 68, 84, 126, and 184 respectively (in units of  $h_{70.4}^{-1} \text{ Mpc}$ ).

Our new determination is higher but statistically consistent with the mean free path estimate of Faucher-Giguère et al. (2008) at comparable redshift. These authors use an independent technique based on an analytic calculation for a given column density distribution function and find  $\lambda_{\text{mfp}}^{912} \sim 85 \text{ Mpc}$  at  $z \sim 3$ . In Figure 5, our new mean free path estimates are also compared to the results of other studies that are based on a similar stacking analysis (Prochaska et al. 2009; O’Meara et al. 2013; Worseck et al. in prep.). This figure shows that the mean free path of ionizing photons in the Universe smoothly evolves between  $z \sim 2.5 - 5.5$ . This redshift evolution is well described analytically by

$$\tau_{\text{eff}}^{LL}(z, z_{\text{qso}}) = \int_0^\infty \int_z^{z_{\text{qso}}} f(N_{\text{HI}}, z') \times (1 - \exp(-N_{\text{HI}}\sigma_{\text{ph}})) dN_{\text{HI}} dz', \quad (13)$$

with  $\sigma_{\text{ph}}$  the frequency-dependent photoionization cross section and  $f(N_{\text{HI}}, z)$  the 5-parameter column density distribution function by O’Meara et al. (2013). Here,  $f(N_{\text{HI}}, z)$  has a redshift invariant shape, but the normalization evolves as a power law of index  $\gamma \sim 1.5 - 2$ , with  $\gamma \sim 2$  slightly favored by the data (see grey dashed line in Figure 5). According to this analytic form, that we normalize to match the observed  $\lambda_{\text{mfp}}^{912}$  at  $z \sim 4$ , photons can freely escape from the emitting sources by  $z \sim 1.4 - 1.8$ , the redshift at which the mean free path of ionizing photons equals the horizon  $h = \int_{r(0)}^{r(z_{\text{qso}})} dr'$ .

Before concluding our discussion on the mean free path, we note that recent work by Rudie et al. (2013) suggests a significantly shorter  $\lambda_{\text{mfp}}^{912}$  at  $z \sim 2.4$  compared

to the estimate of O’Meara et al. (2013). This result would imply a shallower redshift evolution than what is presented in Figure 5. The analysis of Rudie et al. (2013) relies on the measurement of the column density distribution function at  $z \sim 2.4$ , for which discrepant values exist in the literature. Due to the difficulties of measuring individual absorption line systems at column density above  $N_{\text{HI}} \gtrsim 10^{15.5} \text{ cm}^{-2}$  where saturation effects in the strongest lines of the Lyman series arise, we currently prefer the more direct measurements of the mean free path from the stacking analysis.

## 5. A SURVEY OF $\tau \geq 2$ LYMAN LIMIT SYSTEMS

### 5.1. Catalogue of intervening LLSs

We compile a catalogue of intervening LLSs in two steps. First, we perform an automated search for flux discontinuities that can be attributed to absorption at the Lyman limit in the blue portion of the MagE spectra. This is done by comparing the observed flux in bins of  $18\text{\AA}$  to a model for the quasar continuum that is constructed by extrapolating the power law continuum measured at  $> 1215\text{\AA}$  and including absorption from the Lyman- $\alpha$  forest. Starting from the Lyman limit at the quasar redshift and moving blueward, the automatic procedure searches for flux discontinuities that can be modeled with an intervening LLS with  $N_{\text{HI}} \geq 10^{17} \text{ cm}^{-2}$  in steps of redshift  $\Delta z = 0.01$ . Once a flux break is detected, the procedure compares models for the Lyman limit absorption at different column densities (in steps of  $\Delta \log N_{\text{HI}} = 0.1$ ) to identify  $\tau \geq 2$  LLSs. Redshifts and column densities for these systems are stored.

To obtain a clean and complete census of LLSs at  $2.6 \lesssim z \lesssim 3$ , we then inspect each quasar spectrum in search of a sharp flux decrement associated to the Lyman limit in the rest frame of  $\tau \geq 2$  LLSs (e.g. Figure 6.2), starting from the list of systems flagged by the automated search. Three of the authors (MF, JO, XP) have independently modeled the observed quasar flux by superimposing to an underlying continuum level both the Lyman series and the Lyman limits associated to intervening absorption systems. During this procedure, two different methods for establishing the quasar continuum have been adopted. The first method, previously used by

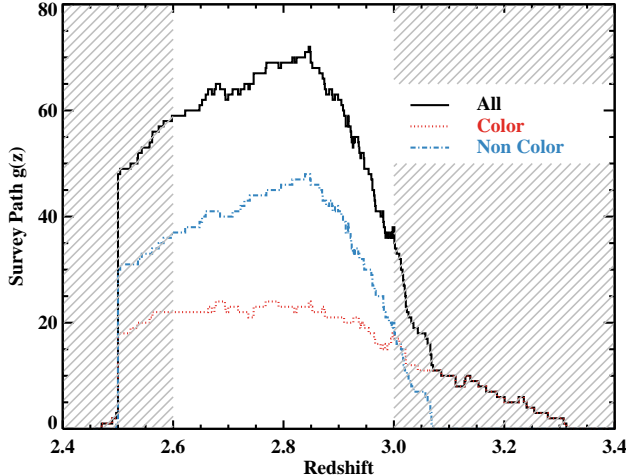


**Figure 7.** Redshift path probed by our MagE survey of  $\tau \geq 2$  LLSs for the full (black solid line), the color selected (red dotted line), and the non-color selected (blue dashed line) samples. The grey shaded area highlights the redshift range excluded from the statistical analysis either because of the limited path ( $z > 3$ ) or because of the lower S/N at  $z < 2.6$ .

O’Meara et al. (2013), relies on the Telfer et al. (2002) composite spectrum, which we adapt to the observed flux by allowing for a scale in normalization and a power law tilt. The second method, instead, assumes an extrapolation of the power law continuum measured at  $> 1215\text{\AA}$ , to which we apply a correction for the Lyman- $\alpha$  forest absorption as described in Section 3. Both methods are found to yield consistent results. We emphasize that during this search, systems are selected purely based on their Lyman limit and Lyman series. Redshifts are determined by means of high order lines in the Lyman series to avoid a possible bias associated to the presence or lack of metal lines. Further, particular attention is given to the transmitted flux blueward of the Lyman limit which is needed to separate LLSs at  $\tau \geq 2$  from those at  $\tau < 2$ .

For the majority of cases (99/105), at least two authors have agreed on the presence and redshift of a  $\tau \geq 2$  LLS. For the remaining 6/105 cases in which discrepant models have been produced, three authors have jointly discussed the best model to describe the data. Not surprisingly, these discrepancies arise mostly at low S/N and blueward of  $\lesssim 3400\text{\AA}$ . We estimate that typical uncertainties of the hydrogen column density at  $N_{\text{HI}} = 10^{17.5} \text{ cm}^{-2}$  range between  $\sim 0.05 - 0.10$  dex, and depend on the spectrum S/N. However, the quality of the data at  $\lesssim 3300\text{\AA}$  quickly worsen, and a much larger uncertainty is associated to systems at  $z < 2.6$ . Because of our limited ability in identifying  $\tau \geq 2$  LLSs at these redshifts, in the following analysis we restrict our statistical survey to  $2.6 \leq z \leq 3.0$ .

We further assess the completeness and purity of our catalogue of LLSs at  $z \geq 2.6$  using mock spectra. One of the authors (GW) generated four independent realizations of MagE spectra for each of the 105 quasars, assuming the same continuum and noise properties of the individual observed spectra and following the procedures detailed in Dall’Aglio et al. (2008), Prochaska et al. (2010), and Worseck & Prochaska (2011). These 420 mock spectra were subsequently analyzed independently by the

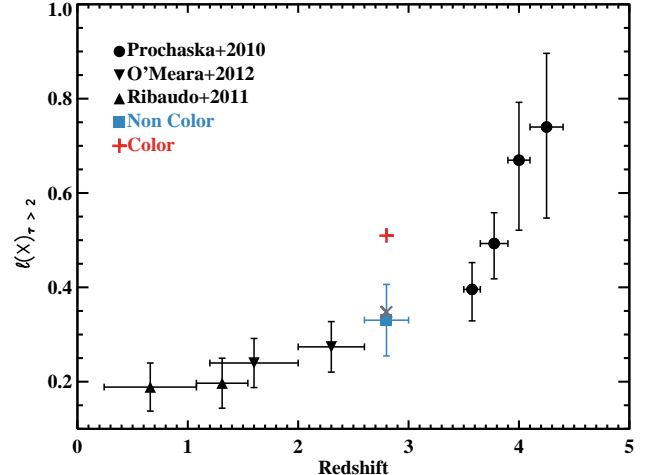


**Figure 8.** Redshift evolution of the number of  $\tau \geq 2$  LLSs per unit redshift. The result of our MagE survey (blue square for the non-color selected sample) is compared to values from the literature (O’Meara et al. 2013; Prochaska et al. 2010; Ribaldo et al. 2011a) at lower and higher redshifts.  $\ell(X)$  measured in the color selected sample is also shown with a red cross. The grey X shows instead the expected value of  $\ell(X)$  computed by extrapolating the O’Meara et al. (2013)  $f(N_{\text{HI}}, X)$  to  $z = 2.8$ . Observations reveal a smooth evolution in the number density of LLSs between  $z \sim 0.5 - 4.5$ .

other three authors (MF, JO, XP), following the same procedures adopted for the real data as described above. Results were then compared to the input catalogue of LLSs. From this comparison, we conclude that in 95% of the cases (398/420 spectra), we are able to either correctly identify the presence of a  $\tau \geq 2$  LLS or to establish that no optically-thick system is present along the line of sight. Further, we successfully identify 189 of the 202  $\tau \geq 2$  LLSs that are embedded in the mock spectra, corresponding to a completeness of 94%. Thanks to the presence of the Lyman series, we are able to characterize the redshift of 90% of the identified LLSs to within  $\delta z = \pm 0.0005$ . Finally, 198 of the 207 systems that we flag as  $\tau \geq 2$  LLSs have in fact a column density  $\log N_{\text{HI}} \geq 17.5$ , corresponding to a purity of 96%. The remaining 9 systems are false positive that have column densities  $17.4 \leq \log N_{\text{HI}} < 17.5$ , corroborating our estimate for the error on the column density of  $\sim 0.05 - 0.1$  dex.

## 5.2. Incidence of LLSs

Having a complete list of LLSs in our sample (Table 2), we can extract a statistical sample to quantify the number of LLSs per unit redshift by imposing additional selection criteria that define the total redshift path  $g(z)$  probed by our MagE survey (Figure 7). First, LLSs with a velocity  $\leq 3000 \text{ km s}^{-1}$  from the quasar redshift are excluded because of their likely physical proximity to the quasar host galaxies. Further, when a  $\tau \geq 2$  LLS is detected at  $z_{\text{lls}}$ , the sharp flux decrement prevent us from searching additional systems at  $z < z_{\text{lls}}$ . Therefore, in each sightline, we consider the redshift range  $2.6 \equiv z_{\text{end}} < z < z_{\text{start}} \equiv z_{\text{qso}} - z_{3000\text{km/s}}$ . If a  $\tau \geq 2$  LLS is detected,  $z_{\text{end}} = z_{\text{lls}}$ , and if  $z_{\text{lls}} > z_{\text{start}}$ ,  $z_{\text{end}} = z_{\text{start}}$ . Finally, because of the limited path of our survey beyond  $z = 3$ , we impose a limit  $z_{\text{start}} \leq 3$ . Individ-

ual values for  $z_{\text{end}}$  and  $z_{\text{start}}$  are summarized in Table 2, where we also highlight quasars that are in common with the previous surveys by Sargent et al. (1989) and Lanzetta (1991). Considering the small overlap (10/105 sightlines), this survey is largely independent from previous efforts at comparable redshifts.

Given the total redshift path of the survey, we define the incidence of  $\tau \geq 2$  LLSs as the total number of systems detected within the useful redshift range divided by the integral of  $g(z)$

$$\ell(z)_{\tau \geq 2} = \frac{N_{\text{lls}}}{\int g(z) dz}. \quad (14)$$

In our statistical sample between  $2.6 \leq z \leq 3$ , we find  $\ell(z)_{\tau \geq 2} = 1.21 \pm 0.28$  for the non-color selected sample and  $\bar{\ell}(z)_{\tau \geq 2} = 1.86 \pm 0.46$  for the color selected sample. Here, the uncertainties are related to counting errors only. As previously found for the mean free path (Figure 3), there is a systematic difference between the color and non-color selected samples, albeit the two values of  $\ell(z)$  are marginally consistent due to the large uncertainties.

For the assumed cosmological model, we can further use the identity  $\ell(z)dz = \ell(X)dX$  to recast the observed number of LLSs per unit redshift into a more physically motivated quantity that is proportional to the comoving number density of LLSs times their physical cross section (e.g. Bahcall & Peebles 1969). In this transformation,

$$dX = \frac{(1+z)^2 dz}{\sqrt{\Omega_{\Lambda} + \Omega_{\text{m}}(1+z)^3}}, \quad (15)$$

and given that  $dz/dX = 0.27$  at  $z = 2.8$ , we find  $\ell(X)_{\tau \geq 2} = 0.33 \pm 0.08$  and  $\bar{\ell}(X)_{\tau \geq 2} = 0.51 \pm 0.13$  for the non-color and color selected samples, respectively. In Figure 8, the results from our survey (blue square and red cross) are compared to previous determinations of  $\ell(X)$  in samples of  $\tau \geq 2$  LLSs that have been selected within narrow intervals of redshift (Prochaska et al. 2010; Ribaudo et al. 2011a; O’Meara et al. 2013). Here, we also show the predicted  $\ell(X)$  at  $z = 2.8$  (grey X) that we compute from an extrapolation of the O’Meara et al. (2013)  $f(N_{\text{HI}}, X)$  assuming  $\ell(z) \sim (1+z)^{1.5}$ . The almost perfect agreement, consistent with what we previously found in the mean free path evolution, validate our previous assumption in constructing a model for the Lyman- $\alpha$  forest (see Section 4).

Finally, we estimate the contribution of  $\tau \geq 2$  LLSs to the observed  $\lambda_{\text{mfp}}^{912}$ . By definition,

$$\ell(X) = \frac{c}{H_0} n_c(z) \phi(z) \quad (16)$$

with  $n_c$  the comoving number density of LLSs and  $\phi$  their physical cross section. At  $z \sim 2.8$ , the typical separation between LLSs therefore becomes (e.g. Ribaudo et al. 2011a)

$$\lambda_{\text{lls}} = \frac{c}{H_0(1+z)^3 \ell(X)} \sim 235 \text{ Mpc}. \quad (17)$$

Compared to  $\lambda_{\text{mfp}}^{912} = 100 \pm 29 \text{ h}_{70.4}^{-1} \text{ Mpc}$ , it follows that systems with  $N_{\text{HI}} \geq 10^{17.5} \text{ cm}^{-2}$  account for only 40% of the observed mean free path. Similarly, integrating Equation 13 between  $z_{\text{qso}} = 3.01$  and  $z_{912} = 2.651$ , we

find that  $\tau \geq 2$  LLSs contribute to 43% of the total Lyman limit optical depth for the assumed O’Meara et al. (2013)  $f(N_{\text{HI}}, X)$ . All together, our analysis reveals properties for the mean free path and for the number of  $\tau \geq 2$  LLSs that are consistent with previous determinations at other redshifts, implying a smooth evolution of the optically thick gas distribution across  $\sim 9$  Gyr of cosmic history.

## 6. PHYSICAL PROPERTIES OF LYMAN LIMIT SYSTEMS

In this section, we exploit the quality of our MagE spectra to investigate the physical properties of  $\tau \geq 2$  LLSs. Here, we focus our analysis on a composite spectrum of LLSs to qualitatively explore typical values of metallicity and ionization parameters in a representative ensemble of systems that are selected purely based on their hydrogen column density between  $2.6 \leq z \leq 3$ . A detailed analysis of the physical conditions in individual LLSs is deferred to future work.

In the previous sections, we showed how the number of LLSs found in color selected samples exceeds the number of intervening systems along non-color selected quasars. As discussed, this bias is due to the fact that absorption at the Lyman limit reddens the colors of these quasars, that are preferentially selected for spectroscopic follow-up because they separate from the stellar locus. Additional reddening may come from dust (Vladilo et al. 2006; Kaplan et al. 2010), but studies of damped Lyman- $\alpha$  systems (DLAs), at even higher column densities of  $N_{\text{HI}} \geq 10^{20.3} \text{ cm}^{-2}$ , suggest only modest differences in the reddening of optical and radio selected quasars with intervening DLAs (Jorgenson et al. 2006). Thus, given two LLSs along a color selected quasar and a non-color selected quasar, there is no current indication that they will have largely different physical properties (e.g. their metal content), except perhaps an higher  $N_{\text{HI}}$  column density for the systems along color selected quasars. For this reason, in the remainder of this work, we combine the two populations of LLSs detected along color and non-color selected samples.

### 6.1. The composite LLS spectrum

To generate a composite spectrum of  $z \sim 2.8$  LLSs, we first continuum normalize the quasar spectra by fitting a polynomial function to the data redward to the quasar Lyman- $\alpha$  emission lines, omitting regions where metal lines are detected in absorption. At wavelengths blueward to Lyman- $\alpha$ , instead, we generate a continuum model using a spline function that is constrained by the data in regions free from evident absorption arising in intervening systems. Between the quasar Lyman- $\alpha$  and Lyman- $\beta$  emission lines, we further adopt a first guess for the continuum level using principle component analysis, following the procedure described in P aris et al. (2011). Next, we median combine the normalized spectra in the rest-frame of the 38  $\tau \geq 2$  LLSs that are part of our statistical sample at  $z \geq 2.6$ . In this case, a median is preferred over the arithmetic mean to attempt to preserve the definition of optical depth associated to each absorption line. As previously done for the quasar composite spectrum, the error array is derived via bootstrapping.

The LLS composite spectrum is shown in Figure 9, where we mark the position of metal transitions that



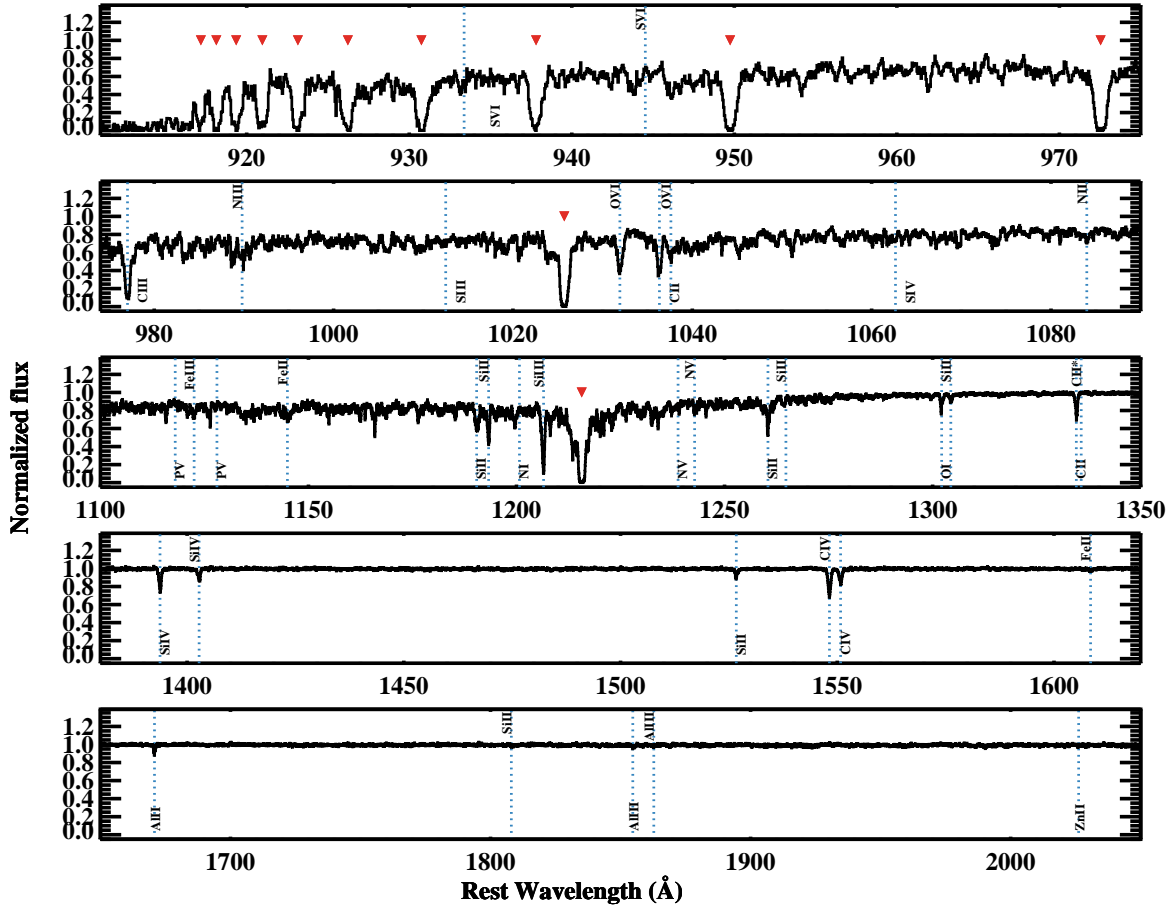


**Figure 9.** Composite spectrum of 38  $\tau \geq 2$  LLSs which are included in our statistical sample at  $z \geq 2.6$ . Hydrogen lines in the Lyman series are detected through Ly13 and are marked by red triangles. The position of common metal absorption lines is also highlighted with blue dotted vertical lines. Spectra of LLSs are characterized by multiple absorption lines associated to metals in different ionization states, most notably C III and Si III.

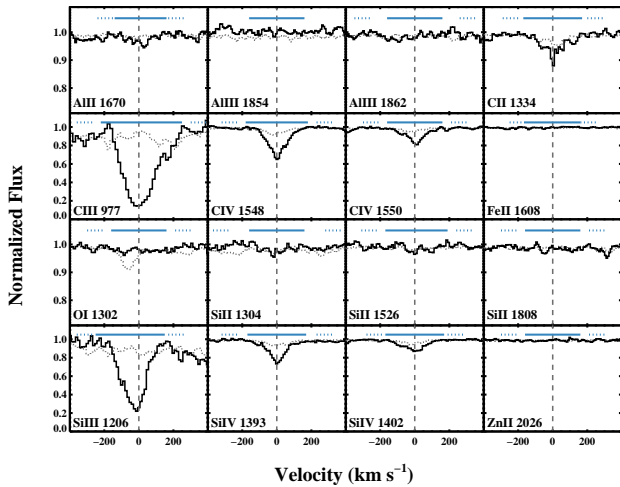


**Figure 10.** Velocity plot of selected metal lines that are included in the photo-ionization modeling of a composite spectrum of 20 LLSs with  $\log N_{\text{HI}} = 17.5 - 19.0$ . In grey, we show the associated errors, which we compute via bootstrapping. The solid and dotted blue lines at the top of each panel mark the velocity windows used to compute the line equivalent widths and the local continuum, respectively. At  $\log N_{\text{HI}} < 19.0$ , only doubly and triply ionized metal ions are most evident.

are common in intervening systems. Besides the prominent hydrogen Lyman series, multiple transitions in different ionization states are detected, including O VI, Si IV and C IV, strong C III and Si III, singly ionized Si, C, Al, and O I. Similar absorption lines have been reported in a composite spectrum of LLSs at  $z \sim 3.5$  (Prochaska et al. 2010). Although systems with  $N_{\text{HI}} \geq 10^{19} \text{ cm}^{-2}$  are formally classified as LLSs, several studies have already investigated the typical metallicity and ionization state of DLAs with  $N_{\text{HI}} \geq 10^{20.3} \text{ cm}^{-2}$  and of sub-DLAs or super-LLSs (SLLSs) with  $N_{\text{HI}} = 10^{19} - 10^{20.3} \text{ cm}^{-2}$  (e.g. Dessauges-Zavadsky et al. 2003; Rafelski et al. 2012). Conversely, with the exception of the pioneering study of Steidel (1990), the metal properties and ionization states of  $z \sim 3$  LLSs with  $N_{\text{HI}} = 10^{17.5} - 10^{19} \text{ cm}^{-2}$  have been investigated in only a handful of systems (see appendix of Fumagalli et al. 2011b) and a detailed study of a homogeneous and unbiased sample of LLSs is at present lacking.

To explore the metal absorption properties of this subclass of LLSs, we generate a second composite spectrum for the 20  $\tau \geq 2$  LLSs in our statistical samples that exhibit an H I column density  $< 10^{19} \text{ cm}^{-2}$ , as inferred from the absence of damping wings in the Lyman- $\alpha$  line profile. In Figure 10, we show the line profiles of common metal transitions in this second composite spectrum

at  $\lambda > 1300\text{\AA}$ . Other transitions are detected at even shorter wavelength, but because of the limited sample size and the increasingly high contamination from the Lyman- $\alpha$  forest blueward to  $\lambda = 1300\text{\AA}$ , blends significantly affect our ability to reliably measure equivalent widths. However, given the predominance of doubly ionized transitions in LLSs (see Figure 9 or, e.g. Ribaldo et al. 2011b) and the fact that C III  $\lambda 977\text{\AA}$  and Si III  $\lambda 1206\text{\AA}$  are clearly detected in the stack, we also include these transitions in our analysis. The most evident feature of Figure 10 is that, compared to the stack of all LLSs, the singly ionized species and O I are mostly undetected. A similar dichotomy between lower and higher ionization lines at different densities has been reported by Pieri et al. (2010) in a composite spectrum of strong Lyman- $\alpha$  forest absorbers, with  $N_{\text{HI}} \gtrsim 10^{15.4} \text{ cm}^{-2}$ .

To characterize the strength of the selected metal lines in the composite spectrum, we measure the line equivalent widths  $W$  within a velocity window that is large enough to encompass the entire line profile. For the undetected lines, we fix instead the velocity window at  $\pm 160 \text{ km s}^{-1}$ , comparable to the width of the detected lines. A summary of these measurements is provided in Table 3, where we list  $3\sigma$  limits for non detections.

Given the suggested connection between LLSs and the halo gas in the surroundings of galaxies (see Section 7), we compare the typical equivalent widths observed in LLSs and in the circumgalactic medium (CGM) of galaxies at similar redshifts. Using a composite of galaxy spectra at low resolution, Steidel et al. (2010) have derived the typical equivalent widths of C II, Si IV, and C IV in the CGM of  $z \sim 2 - 3$  galaxies. The equivalent widths for LLSs are comparable to the values reported for the CGM only at the largest impact parameters, beyond  $\sim 80 - 100 \text{ kpc}$  from the galaxy centers. At face value, this result implies that the majority of LLSs with  $N_{\text{HI}} = 10^{17.5} - 10^{19} \text{ cm}^{-2}$  do not arise from the innermost CGM of Lyman break galaxies (LBGs) with  $L \gtrsim 0.3L_*$ . However, this seems in contradiction to the empirical result that the halos of LBGs contain enough neutral gas to account for a significant fraction of the population of  $\tau \geq 2$  LLSs within  $\sim 100 \text{ kpc}$  from the galaxy centers (Steidel et al. 2010). This tension reveals a still incomplete understanding on the gas distribution around LBGs in connection to the population of LLSs, a gap that future studies need to address.

## 6.2. Photo-ionization modeling

In this section, we use photo-ionization modeling to qualitatively investigate the typical metallicity and ionization conditions that are required to reproduce the equivalent widths seen in the composite spectrum of LLSs with  $\log N_{\text{HI}} = 17.5 - 19.0$  at  $z \sim 2.8$ .

As evident from Figure 10, the majority of the metal transitions in this composite spectrum lie on the linear portion of the curve of growth, with the exception of C III and Si III that are most likely saturated at the spectral resolution of MagE. We can therefore directly map the observed equivalent widths into column densities, as listed in Table 3. Consistent values of column densities are also found via the apparent optical depth method (Savage & Sembach 1991). Before proceeding, we emphasize that several effects confound the physical

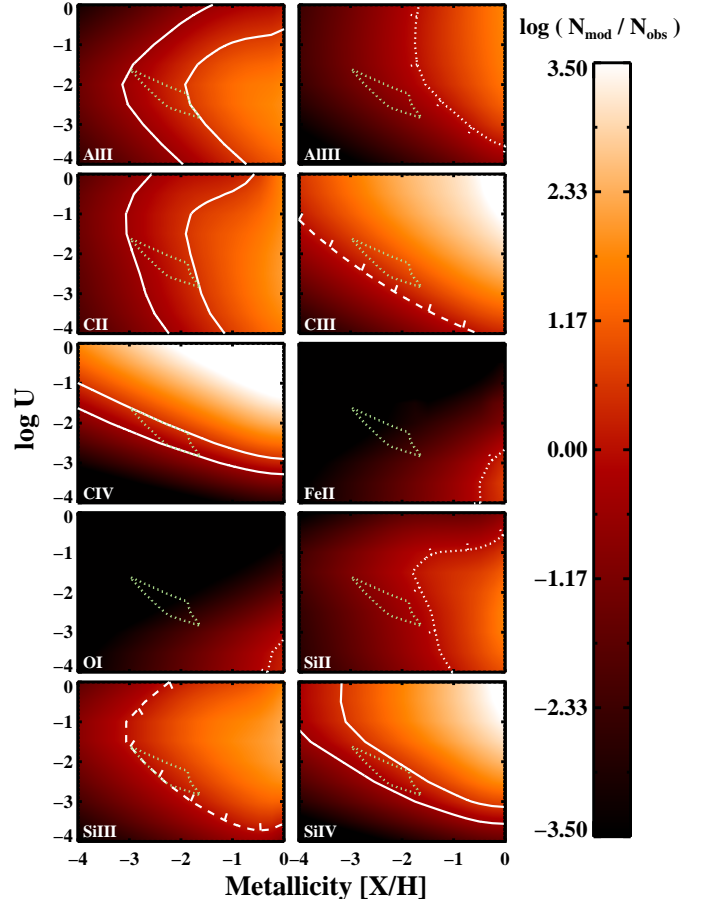


**Figure 11.** Results from the photo-ionization modeling of the composite spectrum of  $\log N_{\text{HI}} = 17.5 - 19.0$  LLSs. In each panel, we compare the observed line strength of selected metal transitions to model predictions at different metallicities and ionization parameters. For each ion, the range of parameters that are consistent with the observed equivalent widths is marked by two solid white lines. For lower and upper limits, we show instead the allowed parameter space with dashed and dotted lines, respectively. The green dotted lines enclose the typical metallicity and ionization parameter that qualitatively reproduce the metal line strengths in the composite spectrum. Note that the left edge of this region is formally a lower limit. Our analysis reveals a population of ionized and likely metal poor systems.

interpretation of column densities measured in composite spectra, including contamination from unrelated absorption lines or offsets in velocity between metal transitions and the systemic redshifts measured from hydrogen lines. Moreover, differential dust depletion and variation in the radiation field to which individual systems are exposed (see e.g. Cooke et al. 2013) complicate the interpretation of the measured column densities. Therefore, the listed column densities will be used only as proxy for the equivalent widths to gain qualitative insight on the physical properties of  $z \sim 2.8$  LLSs. A detailed analysis of individual systems will be presented in future work.

Results from the photo-ionization modeling are summarized in Figure 11, where we show the column densities of metal transitions as a function of  $U$  and  $[\text{Fe}/\text{H}]$ , normalized to the observed column densities or the corresponding limits listed in Table 3. Models are computed using the CLOUDY (v10.00) photo-

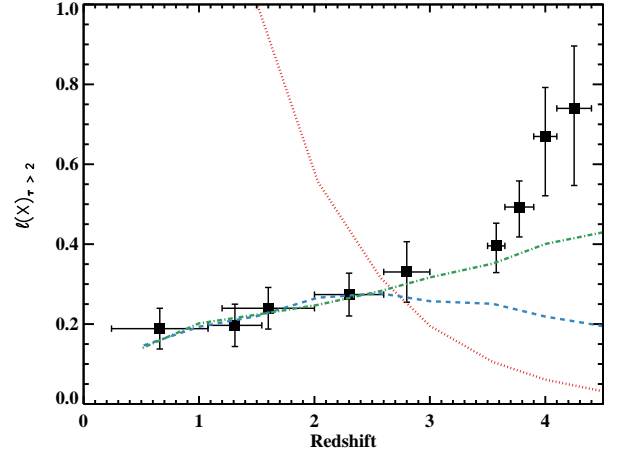
ionization code (Ferland et al. 1998), including both collisional ionization and photo-ionization at equilibrium and the Haardt & Madau (2012) extragalactic UV background at  $z \sim 2.8$ . During our analysis, relative abundances of different elements are fixed to the solar values (Asplund et al. 2009). We also assume a typical hydrogen column density of  $\log N_{\text{HI}} \sim 17.8$ , a value that is consistent with the median column density derived in random realizations of 20 LLSs that are drawn from the O’Meara et al. (2013)  $f(N, X)$  at  $z \sim 2.8$  between  $\log N_{\text{HI}} = 17.5 - 19.0$ . Further, the flux transmitted blueward to the Lyman limit is also consistent with a median  $\log N_{\text{HI}} \geq 17.8$ .

Figure 11 reveals how the doubly and triply ionized C and Si transitions provide the most stringent constraints for the  $U$  parameter, but they are mostly insensitive to the metallicity of the gas. Conversely, C II and Al II are the most constraining transitions for the metallicity, although degenerate with respect to  $U$ . Combining all the independent constraints, we conclude that the equivalent widths observed in the composite spectrum of  $\log N_{\text{HI}} = 17.5 - 19.0$  LLSs can be reproduced by gas that is significantly ionized ( $\log U \gtrsim -3$ ), and likely metal poor ( $[\text{Fe}/\text{H}] \lesssim -1.5$ ) (cf. Steidel 1990; Prochaska & Burles 1999). We should again emphasize that the use of the median composite spectrum to describe the entire population of LLSs is rather simplistic, as it does not capture information on the shape of the distribution. This is especially relevant given the recent claim by Lehner et al. (2013) of a bimodal distribution of the metallicity in LLSs at  $z \lesssim 1$ , with one population peaking around  $[\text{X}/\text{H}] \sim -1.5$  and a second population centered at  $[\text{X}/\text{H}] \sim -0.3$ .

Our qualitative analysis suggests that LLSs are probably more enriched than the IGM at  $[\text{C}/\text{H}] \sim -3$  (e.g. Simcoe 2011), and possibly enriched to  $[\text{X}/\text{H}] \sim -1.5$ , the median metallicity observed in DLAs (e.g. Rafelski et al. 2012). Assuming a general picture of an increasingly higher metallicity in regions that are progressively closer to the site of star formation, where metals are produced, the enhanced metallicity of LLSs places this population of absorbers in proximity to or within galaxies halos that have been at least in part enriched by metals ejected from galaxies (e.g. Shen et al. 2013).

## 7. LYMAN LIMIT SYSTEMS AND GALAXY HALOS

In this last section, we expand the discussion of the connection between galaxies and LLSs, to which we alluded in the previous sections. Already from the first quasar surveys, it became evident how LLSs differ from the Lyman- $\alpha$  forest (Tytler 1982; Sargent et al. 1989; Steidel 1990) and that these absorbers are likely connected to galaxies. This idea has been subsequently reinforced by modern studies of the CGM (e.g. Steidel et al. 2010; Chen et al. 2010; Prochaska et al. 2011; Rudie et al. 2012; Werk et al. 2013; Churchill et al. 2013; Prochaska et al. 2013; Stocke et al. 2013) that show how cold, enriched, and partially ionized gas from which LLSs can originate fills galaxy halos both in the local and distant Universe. At the same time, several theoretical studies have addressed the connection between LLSs and galaxies in the high redshift Universe (e.g. Katz et al. 1996; Gardner et al. 2001; Kohler & Gnedin 2007; Faucher-Giguère & Kereš 2011; Fumagalli et al.



**Figure 12.** Models for the observed evolution of  $\ell(X)$  for  $\tau \geq 2$  LLSs (black squares). A “minimal model” in which halos within a redshift-independent mass range contribute to the number of LLSs proportionally to their virial area is shown with a red dotted line. This model drastically fails to reproduce the observed  $\ell(X)$ . The “wind model” composed by halos above a critical mass at which ejecta from supernovae do not escape the halos is shown with a blue dashed line. This model can account for observations at  $z \lesssim 3$  only under the ansatz that the cross section of the circumgalactic medium is redshift independent. The “accretion model” composed by halos that are rare fluctuations in the density field is superimposed with a green dash-dotted line. This model describes the observed  $\ell(X)$  up to  $z \sim 3.5$  without any prior assumption on the size of the circumgalactic medium.

2011a; Altay et al. 2011; van de Voort et al. 2012; Fumagalli et al. 2013; Rahmati et al. 2013). Consistent findings are that LLSs arise from galaxy halos, in a mixture of infalling, static, and outflowing gas.

Having a complete view of the redshift distribution of LLSs across nearly  $\sim 10$  Gyr of cosmic history (Figure 8), we explore with simple toy models how the evolution of  $\ell(X)$  relates to the evolution of the gas within galaxy halos. Similar investigations have been carried out in the literature by several authors. Recently, Ribaud et al. (2011a) adopted an empirical approach to describe the evolution of LLSs in terms of the galaxy luminosity function and size-luminosity relation. These authors concluded that to account for the observed redshift dependence of  $\ell(X)$ , galaxies with  $L < L_*$  have to contribute to the population of LLSs and that the physical cross section of the absorbing material rapidly evolves from  $z \sim 5$  to  $z \sim 2$ , remaining relatively constant afterwards. While instructive and empirical, this calculation does not provide a direct link between the halos in which galaxies resides and the incidence of LLSs. In this work, we revise this open question and propose possible scenarios for the co-evolution of LLSs and galaxy halos that is empirically traced by the redshift evolution of  $\ell(X)$ .

We construct a simple toy model of the Universe which we populate with dark matter halos with comoving number density  $n_{\text{gal}}(M_{\text{vir}}, z)$ . In our calculation, we assume a Sheth-Tormen halo mass function (Sheth & Tormen 1999) computed as described in Dekel & Birnboim (2006) and corrected to match the results of the Bolshoi simulation (Klypin et al. 2011). We then assign to each halo a characteristic virial radius  $R_{\text{vir}}(M_{\text{vir}}, z)$ , using redshift dependent scaling relations derived from the ROCKSTAR halo catalogues

(Behroozi et al. 2013a,b) extracted from the Bolshoi simulation. Following the definition of  $\ell(X)$  in Equation (16), we compute the galaxy contribution to the observed  $\ell(X)$  as

$$\ell(X) = \frac{4c\pi}{H_0} \int_{\log M_{\text{low}}}^{\log M_{\text{up}}} R_{\text{vir}}^2(M_{\text{vir}}, z) f_c(M_{\text{vir}}, z) \frac{dn_{\text{gal}}}{d \log M_{\text{vir}}}(M_{\text{vir}}, z) d \log M_{\text{vir}} \quad (18)$$

with  $\log M_{\text{up}}$  and  $\log M_{\text{low}}$  the upper and lower mass limits and  $f_c$  the covering factor of  $\tau \geq 2$  LLSs within twice the virial radius. Despite this formal definition, for a given cosmology,  $\ell(X)$  is only constraining  $f_c \times R_{\text{vir}}^2$ , and it should be noted that we cannot discriminate between, e.g., a 10% covering factor within twice the virial radius and a 40% covering factor within one virial radius.

In this model, while  $M_{\text{vir}}$  and  $R_{\text{vir}}$  are fixed by the adopted cosmology,  $\log M_{\text{up}}$ ,  $\log M_{\text{low}}$ , and  $f_c$  are free parameters that may vary as a function of redshift and halo mass. The intrinsically one-dimensional nature of absorption line surveys is currently unable to disentangle the relative contribution of these parameters and, for this reason, we restrict to a minimal set of variables. First, we fix the upper limit  $\log M_{\text{up}} = 13$  to mimic the formation of a hot halo above a critical halo mass at which virial shocks become stable (e.g. Dekel & Birnboim 2006). This limit is higher than the typical value quoted for this critical halo mass (between  $\sim 10^{11-12} M_{\odot}$ ) to account for recent observational results which show a substantial amount of cold gas at or even beyond the mass scale at which hot halos are postulated to develop (Prochaska et al. 2013; Churchill et al. 2013). However, because of the low number density of high mass halos, our result is largely insensitive to the assumed upper mass limit above  $\log M_{\text{up}} \sim 12.5$ . The second simplifying assumption is that, lacking strong priors for the functional form of  $f_c(M_{\text{vir}}, z)$ , we assume a constant covering factor both in redshift and within the mass range specified by  $\log M_{\text{up}}$  and  $\log M_{\text{low}}$ . Thus, in our toy model,  $f_c$  merely sets the absolute normalization of the predicted  $\ell(X)$ . Validation of this assumption awaits future theoretical and observational work.

The first model we construct, which we dub “minimal”, assumes that all the halos in the mass range  $\log M_{\text{up}} = 11$   $\log M_{\text{low}} = 13$  contribute to the observed  $\ell(X)$  proportionally to their virial area ( $A_{\text{vir}} \propto R_{\text{vir}}^2 \propto M_{\text{vir}}^{2/3}$ ). As shown in Figure 12, a choice of  $f_c \sim 0.15$  at twice the virial radius ensures that this minimal model (red dotted line) matches the observed incidence of LLSs around  $z \sim 2.5$ . This covering factor lies in between theoretical predictions at comparable redshifts (Fumagalli et al. 2011a; Faucher-Giguère & Kereš 2011; Shen et al. 2013; Fumagalli et al. 2013) and what is inferred around LBGs (Rudie et al. 2012) and quasar host galaxies (Prochaska et al. 2013).

The most evident problem with the minimal model is a complete inconsistency in the redshift evolution of  $\ell(X)$ . This failure cannot be resolved with simple scaling of  $f_c$  and originates from an increase of almost a factor of  $\sim 20$  in the virial area at fixed halo mass between  $z \sim 0.5 - 5.5$ , combined with an increase of a factor of  $\sim 10$  in the number density of halos across a comparable redshift

range. In principle, this tension could be resolved by assuming that LLSs do not co-evolve with the properties of halo gas. However, given the discussion presented in the previous sections, we believe that this explanation is unlikely, and attribute instead the mismatch between observations and the minimal model to having assumed that LLSs trace the CGM of a galaxy population with fixed halo mass at all redshifts. In the following, we present two possible ways to resolve the failure of the minimal model, which require either a rapid evolution in the typical mass interval from which LLSs arise, or that the size of the optically thick region around galaxies is decoupled from the size of the virial region.

In the second model, we attempt to overcome the shortcomings of the minimal model by introducing a redshift dependent lower mass limit. If we postulate that the majority of LLSs are associated to gas that is deposited in the halo by a feedback mechanism, we can naturally introduce a lower limit  $\log M_{\text{low}}$  by assuming that halos with circular velocities below  $\sim 100 \text{ km s}^{-1}$  (Dekel & Silk 1986) are not able to retain a significant fraction of the ejected gas. For this reason, we define this second toy model as “wind” model. This additional constraint naturally leads to a mild evolution in the number density of halos that host LLSs between  $z \sim 0.5 - 5$ , accounting for the factor of  $\sim 10$  excess encountered in the minimal model. More specifically, the lower mass limit evolves from  $\log M_{\text{low}} \sim 10.5$  at  $z \sim 6$  to  $\log M_{\text{low}} \sim 11.5$  at  $z \sim 0.5$ . Due to the increasing amplitude of the halo mass function as a function of time, the integrated number density of halos that contribute to LLSs slightly increases at first with redshift. By  $z \sim 2.5$ , instead, due to the progressively higher value of  $\log M_{\text{low}}$ , the number density slightly declines with time.

However, the rapid increase in the virial area as a function of redshift would still cause this model to significantly overproduce LLSs at low redshifts, violating the observed  $\ell(X)$ . A better match to the observations is found if, instead, we fix the size of the CGM to the virial area at  $z \sim 2.5$ . Thanks to this ansatz, and by imposing a covering factor of  $f_c \sim 0.15$ , the wind model can account for the observed  $\ell(X)$  evolution between  $z \sim 0.5 - 3$  (blue dashed line in Figure 12). Having imposed a constant cross section for the CGM over the last  $\sim 10$  Gyr of cosmic evolution, this model has only limited predictive power. Nevertheless, it is interesting to note that similar conclusions of an invariant size of the CGM have been reached independently by other studies of absorption line systems (e.g. Chen 2012; Prochaska et al. 2013).

Given the multiple parameters that define  $\ell(X)$  in Equation 18, other models that reproduce the observed incidence of LLSs can be constructed with a different set of assumptions. For instance, a model in which  $\log M_{\text{low}}$  rapidly increases with decreasing redshifts would naturally compensate the growth of the virial area by imposing that LLSs arise from progressively more massive and rarer halos at later times. Conveniently, cosmology offers a way to impose a rapid redshift evolution for  $\log M_{\text{low}}$ . If we postulate that, as suggested by simulations (Fumagalli et al. 2011a; van de Voort et al. 2012), a significant fraction of LLSs arise from dense streams of infalling gas that penetrate inside halos, we can construct a third “accretion” model where  $\log M_{\text{low}}$  is set by a characteristic halo mass  $M_*$  above which halos are

significant fluctuations in the density field. Below this critical mass, halos reside within individual filaments of the cosmic web, where densities are comparable to the virial densities (Dekel & Birnboim 2006). Therefore, below this mass threshold, we postulate that the typical gas densities are below what is required to form LLSs.

By imposing the condition  $\log M_{\text{low}} \geq \log M_*$ , the accretion model (green dash dotted line in Figure 12) accounts for the observed redshift evolution of LLSs, without requiring any adjustment in the spatial extent of the CGM. In this model, however, the inclusion of low mass halos (down to  $M \sim M_*$ ) forces us to adopt a lower covering factor than what was assumed in previous models ( $f_c \sim 0.1$  within virial radius). While the actual value of  $f_c$  is likely higher at most redshifts, this model provides a qualitative illustration on how the rapid redshift evolution of  $M_*$  relegates LLSs to the CGM of progressively rarer halos, thus compensating for the large increase in the virial area at fixed halo mass with cosmic time.

Finally, Figure 12 further illustrates that none of the proposed toy models is able to reproduce the steep rise in  $\ell(X)$  beyond  $z \sim 3.5$ . Clearly, a sudden increase in the extent of the CGM for  $z \gtrsim 3.5$  would reproduce the observed trend (Ribaudo et al. 2011a). However, it is unclear why  $z \sim 3.5$  should represent a special epoch in the evolution of the CGM. Instead, we argue that the different redshift evolution that is observed for  $\ell(X)$  is associated to an increasingly higher contribution of the IGM to the population of LLSs. This is because at progressively higher redshifts the overdensities at which LLSs form approach and exceed the halo virial density and, furthermore, the extragalactic UV background decreases.

A simple calculation can be used to illustrate this argument. For clouds illuminated by UV background radiation, hydrogen densities around  $\sim 0.01 \text{ cm}^{-3}$  are required for the gas to retain  $> 1\%$  of neutral hydrogen (e.g. Appendix B of Fumagalli et al. 2011a). This threshold is comparable to the virial densities of halos at  $z \sim 2.5$ , while by redshift  $z \sim 4$ , typical virial densities equal  $\sim 0.03 \text{ cm}^{-3}$ , the value at which the neutral fraction approaches 30% for a constant UV background. A similar picture is also supported by detailed radiative transfer calculations in numerical simulations that are able to reproduce the abundance of LLSs between  $z \sim 3 - 6$  (McQuinn et al. 2011).

## 8. SUMMARY AND CONCLUSIONS

In this paper, we have presented results of a survey of 105 quasars at  $z \sim 3.0 \pm 0.2$  conducted with the blue sensitive MagE spectrograph at the Magellan Clay telescope. The high signal-to-noise and moderate resolution data have been analyzed to investigate the properties of optically-thick hydrogen at  $z \sim 2.6 - 3$ , a redshift interval that has been not studied in a systematic way by previous surveys. Our principal findings can be summarized as it follows.

- By modeling the composite spectrum of quasars that are selected independently of their optical colors, we have estimated the mean free path of ionizing photons to be  $\lambda_{\text{mfp}}^{912} = 100 \pm 29 \text{ h}_{70.4}^{-1} \text{ Mpc}$  in the  $z \sim 3$  Universe. This value, together with previous determinations at different redshifts from the literature, favors a redshift evolution of in the

amplitude of the column density distribution function in the form  $\sim (1+z)^{1.5-2}$ , and implies that the Universe becomes transparent to ionizing radiation around redshift  $z \sim 1.4 - 1.8$ . During this analysis, we have also confirmed the presence of a previously discovered selection bias in SDSS that systematically misses blue quasars in proximity to the stellar locus.

- We have conducted a survey of  $\tau \geq 2$  LLSs in the wavelength range  $\lambda \sim 3200 - 3800 \text{ \AA}$  and we have characterized the number of LLSs per unit redshift  $\ell(z) = 1.21 \pm 0.28$  at  $z \sim 2.8$ . For the adopted cosmological model, this quantity translates into  $\ell(X) = 0.33 \pm 0.08$ . Our new determination is fully consistent with previous measurements at lower and higher redshifts, implying a smooth evolution of  $\ell(X)$  between  $z \sim 4.5$  and  $z \sim 0.5$ . Combined with our measurement of the mean free path at the same redshift, we have concluded that LLSs with  $\log N_{\text{HI}} \geq 17.5 \text{ cm}^{-2}$  contribute to  $\sim 40\%$  of total mean free path at  $z \sim 3$ .
- With the aid of photo-ionization modeling, we have inferred that a population of ionized ( $U \gtrsim -3$ ) and likely metal poor ( $[X/H] \lesssim -1.5$ ) LLSs is required to reproduce the metal line equivalent widths observed in a composite spectrum of 20 LLSs with  $\log N_{\text{HI}} \sim 17.5 - 19 \text{ cm}^{-2}$  at  $z \sim 2.8$ .
- We have proposed three simple toy models to describe the redshift evolution of  $\tau \geq 2$  LLSs in connection to galaxies. Our main finding is that a model in which LLSs arise in halos of fixed mass at all redshifts drastically fails to reproduce the observed number of LLSs per unit redshift. Successful models require either a rapid redshift evolution of the minimum mass at which LLSs form or a redshift invariant spatial extent of the CGM in the last  $\sim 10$  Gyr of cosmic evolution. In all cases, however, the rapid evolution observed in  $\ell(X)$  at  $z \geq 3.5$  is not accounted for, and we speculate that an increasingly higher contribution from gas within the IGM is required.

In conclusion, our MagE survey of  $z \sim 3$  quasars has provided the missing pieces in a consistent picture of the cosmological evolution of optically thick gas between  $z \sim 0.5 - 4.5$ . The redshift evolution of the mean free path of ionizing radiation and the incidence of  $\tau \geq 2$  LLSs are now well characterized with homogeneous techniques across  $\sim 10$  Gyr of cosmic history, albeit with some controversy at  $z \sim 2.5$ . Our survey has also provided a homogeneous sample of hydrogen-selected LLSs that can be exploited to characterize the physical properties these absorbers and their connections to galaxies at  $z \sim 2.6 - 3$ . The analysis presented in this paper has offered only a first glimpse of the typical metallicity of LLSs, together with viable ways to model the observed evolution of  $\ell(X)$ . Clearly, our work does not provide the final answer to some of the riddles we encountered along the way, including the lower equivalent widths of metal lines in a composite of LLSs compared to what measured in a composite spectrum of galaxies. The task of formulating a coherent picture for the co-evolution of galaxies

and LLSs is therefore a challenge that future studies will have to undertake.

We wish to dedicate this work to the memory of Wallace Sargent for his great contribution to our modern view of LLSs in the distant universe. It is a pleasure to thank A. Dekel and M. Rauch for insightful comments, and A. Cucchiara for collecting the KAST spectra discussed in this paper. We also thank the anonymous referee for comments and criticisms that helped improving this paper. Support for M.F. was provided by NASA through Hubble Fellowship grant HF-51305.01-A awarded by the Space Telescope Science Institute, which is operated by the Association of Universities for Research in Astronomy, Inc., for NASA, under contract NAS 5-26555. Some of observations presented in this paper were collected as part of two NOAO proposals (2010B-0424 and 2009B-0394; PI: JMO). JMO also acknowledges travel support from the VPAA office at Saint Michael's College. JXP acknowledges support from NSF grants AST 10-10004 and AST 11-09447. We acknowledge the use of the Sloan Digital Sky Survey (<http://www.sdss.org/>).

#### REFERENCES

- Altay, G., Theuns, T., Schaye, J., Crighton, N. H. M., & Dalla Vecchia, C. 2011, *ApJ*, 737, L37
- Asplund, M., Grevesse, N., Sauval, A. J., & Scott, P. 2009, *ARA&A*, 47, 481
- Bahcall, J. N., & Peebles, P. J. E. 1969, *ApJ*, 156, L7
- Becker, G. D., Hewett, P. C., Worseck, G., & Prochaska, J. X. 2013, *MNRAS*, 430, 2067
- Behroozi, P. S., Wechsler, R. H., & Wu, H.-Y. 2013, *ApJ*, 762, 109
- Behroozi, P. S., Wechsler, R. H., Wu, H.-Y., et al. 2013, *ApJ*, 763, 18
- Bochanski, J. J., Hennawi, J. F., Simcoe, R. A., et al. 2009, *PASP*, 121, 1409
- Bouché, N., Lehnert, M. D., Aguirre, A., Péroux, C., & Bergeron, J. 2007, *MNRAS*, 378, 525
- Chen, H.-W. 2012, *MNRAS*, 427, 1238
- Chen, H.-W., Wild, V., Tinker, J. L., et al. 2010, *ApJ*, 724, L176
- Churchill, C. W., Nielsen, N. M., Kacprzak, G. G., & Trujillo-Gomez, S. 2013, *ApJ*, 763, L42
- Cooke, R., Pettini, M., Jorgenson, R. A., et al. 2013, *MNRAS*, 431, 1625
- Dall'Aglio, A., Wisotzki, L., & Worseck, G. 2008, *A&A*, 491, 465
- Dekel, A., & Birnboim, Y. 2006, *MNRAS*, 368, 2
- Dekel, A., & Silk, J. 1986, *ApJ*, 303, 39
- Dessauges-Zavadsky, M., Péroux, C., Kim, T.-S., D'Odorico, S., & McMahon, R. G. 2003, *MNRAS*, 345, 447
- Faucher-Giguère, C.-A., Lidz, A., Zaldarriaga, M., & Hernquist, L. 2009, *ApJ*, 703, 1416
- Faucher-Giguère, C.-A., & Kereš, D. 2011, *MNRAS*, 412, L118
- Faucher-Giguère, C.-A., Lidz, A., Hernquist, L., & Zaldarriaga, M. 2008, *ApJ*, 688, 85
- Ferland, G. J., Korista, K. T., Verner, D. A., et al. 1998, *PASP*, 110, 761
- Fumagalli, M., Prochaska, J. X., Kasen, D., et al. 2011a, *MNRAS*, 418, 1796
- Fumagalli, M., O'Meara, J. M., & Prochaska, J. X. 2011b, *Science*, 334, 1245
- Fumagalli, M., Hennawi, J. F., Prochaska, J. X., et al. 2013, *arXiv:1308.1669*
- Gardner, J. P., Katz, N., Hernquist, L., & Weinberg, D. H. 2001, *ApJ*, 559, 131
- Haardt, F., & Madau, P. 2012, *ApJ*, 746, 125
- Jorgenson, R. A., Wolfe, A. M., Prochaska, J. X., et al. 2006, *ApJ*, 646, 730
- Kaplan, K. F., Prochaska, J. X., Herbert-Fort, S., Ellison, S. L., & Dessauges-Zavadsky, M. 2010, *PASP*, 122, 619
- Katz, N., Weinberg, D. H., Hernquist, L., & Miralda-Escude, J. 1996, *ApJ*, 457, L57
- Klypin, A. A., Trujillo-Gomez, S., & Primack, J. 2011, *ApJ*, 740, 102
- Kohler, K., & Gnedin, N. Y. 2007, *ApJ*, 655, 685
- Komatsu, E., Smith, K. M., Dunkley, J., et al. 2011, *ApJS*, 192, 18
- Lanzetta, K. M. 1991, *ApJ*, 375, 1
- Lehner, N., Howk, J. C., Tripp, T. M., et al. 2013, *ApJ*, 770, 138
- Madau, P., Haardt, F., & Rees, M. J. 1999, *ApJ*, 514, 648
- Marshall, J. L., Burles, S., Thompson, I. B., et al. 2008, *Proc. SPIE*, 7014
- McQuinn, M., Oh, S. P., & Faucher-Giguère, C.-A. 2011, *ApJ*, 743, 82
- O'Meara, J. M., Prochaska, J. X., Worseck, G., Chen, H.-W., & Madau, P. 2013, *ApJ*, 765, 137
- Pâris, I., Petitjean, P., Aubourg, É., et al. 2012, *A&A*, 548, A66
- Pâris, I., Petitjean, P., Rollinde, E., et al. 2011, *A&A*, 530, A50
- Pieri, M. M., Frank, S., Weinberg, D. H., Mathur, S., & York, D. G. 2010, *ApJ*, 724, L69
- Prochaska, J. X. 1999, *ApJ*, 511, L71
- Prochaska, J. X., Hennawi, J. F., & Simcoe, R. A. 2013, *ApJ*, 762, L19
- Prochaska, J. X., Weiner, B., Chen, H.-W., Mulchaey, J., & Cooksey, K. 2011, *ApJ*, 740, 91
- Prochaska, J. X., O'Meara, J. M., & Worseck, G. 2010, *ApJ*, 718, 392
- Prochaska, J. X., Worseck, G., & O'Meara, J. M. 2009, *ApJ*, 705, L113
- Prochaska, J. X., O'Meara, J. M., Herbert-Fort, S., et al. 2006, *ApJ*, 648, L97
- Prochaska, J. X., & Burles, S. M. 1999, *AJ*, 117, 1957
- Rafelski, M., Wolfe, A. M., Prochaska, J. X., Neeleman, M., & Mendez, A. J. 2012, *ApJ*, 755, 89
- Rahmati, A., Pawlik, A. H., Raičević, M., & Schaye, J. 2013, *MNRAS*, 430, 2427
- Ribaldo, J., Lehner, N., & Howk, J. C. 2011, *ApJ*, 736, 42
- Ribaldo, J., Lehner, N., Howk, J. C., et al. 2011, *ApJ*, 743, 207
- Rudie, G. C., Steidel, C. C., Shapley, A. E., & Pettini, M. 2013, *ApJ*, 769, 146
- Rudie, G. C., Steidel, C. C., Trainor, R. F., et al. 2012, *ApJ*, 750, 67
- Sargent, W. L. W., Steidel, C. C., & Boksenberg, A. 1989, *ApJS*, 69, 703
- Savage, B. D., & Sembach, K. R. 1991, *ApJ*, 379, 245
- Schlegel, D. J., Finkbeiner, D. P., & Davis, M. 1998, *ApJ*, 500, 525
- Schneider, D. P., Richards, G. T., Hall, P. B., et al. 2010, *AJ*, 139, 2360
- Shen, S., Madau, P., Guedes, J., et al. 2013, *ApJ*, 765, 89
- Sheth, R. K., & Tormen, G. 1999, *MNRAS*, 308, 119
- Simcoe, R. A. 2011, *ApJ*, 738, 159
- Songaila, A., & Cowie, L. L. 2010, *ApJ*, 721, 1448
- Steidel, C. C. 1990, *ApJS*, 74, 37
- Steidel, C. C., Erb, D. K., Shapley, A. E., et al. 2010, *ApJ*, 717, 289
- Stengler-Larrea, E. A., Boksenberg, A., Steidel, C. C., et al. 1995, *ApJ*, 444, 64
- Stocke, J. T., Keeney, B. A., Danforth, C. W., et al. 2013, *ApJ*, 763, 148
- Storrie-Lombardi, L. J., McMahon, R. G., Irwin, M. J., & Hazard, C. 1994, *ApJ*, 427, L13
- Telfer, R. C., Zheng, W., Kriss, G. A., & Davidsen, A. F. 2002, *ApJ*, 565, 773
- Tytler, D. 1982, *Nature*, 298, 427
- Vanden Berk, D. E., Richards, G. T., Bauer, A., et al. 2001, *AJ*, 122, 549
- van de Voort, F., Schaye, J., Altay, G., & Theuns, T. 2012, *MNRAS*, 421, 2809
- Vladilo, G., Centurión, M., Levshakov, S. A., et al. 2006, *A&A*, 454, 151
- Werk, J. K., Prochaska, J. X., Thom, C., et al. 2013, *ApJS*, 204, 17
- Worseck, G., & Prochaska, J. X. 2011, *ApJ*, 728, 23
- Worseck et al. 2013, in preparation

**Table 1**  
Logbook of the observations conducted with the MagE spectrograph.

Name	R.A. (J2000)	Dec. (J2000)	$z_{\text{qso}}$	$\sigma_{z,\text{qso}}^{\text{a}}$	$\sigma_{v,\text{qso}}^{\text{b}}$ (km s $^{-1}$ )	Notes <sup>c</sup>	Date (yymmdd)	Exposure (sec)	Slit (")	S/N at 5500Å
FBQSJ0002+0021	00:02:21.11	+00:21:49.3	3.072	0.007	521	NC	120713	3000	0.7	9.7
Q0038-4041	00:40:49.50	-40:25:14.0	2.977	0.009	714	NC	120715	2700	0.7	26.0
LBQS0041-2638	00:43:42.80	-26:22:11.0	3.058	0.007	521	NC	091223	2000	0.7	16.0
LBQS0047-3050	00:50:20.10	-30:34:21.0	2.967	0.007	521	NC	091223	1000	0.7	13.3
UM669	01:05:16.80	-18:46:42.0	3.041	0.007	521	NC	091223	1000	0.7	20.1
Q0130-403	01:33:01.90	-40:06:28.0	3.031	0.007	521	NC	091222	1200	0.7	30.3
UM148	01:56:36.00	+04:45:28.0	3.001	0.007	521	NC	091223	1000	0.7	14.1
CTS0418	02:17:41.80	-37:01:00.0	2.916	0.007	521	NC	091222	900	0.7	26.2
H0216+0803	02:18:57.30	+08:17:28.0	3.001	0.010	714	NC	100814	1200	0.7	20.4
CTS0220	02:41:22.70	-36:33:19.0	3.109	0.007	521	NC	091223	900	0.7	16.2
Q0244-302	02:46:34.20	-30:04:55.0	3.088	0.007	521	NC	091222	1000	0.7	11.2
CTS0424	03:16:43.80	-56:51:45.0	3.036	0.007	521	NC	091222/23	2200	0.7	32.4
CTS0238	03:30:10.30	-46:26:15.0	3.112	0.007	521	NC	091222	1100	0.7	15.1
Q0351-3740	03:53:08.50	-37:40:54.0	2.952	0.007	521	NC	091222	1200	0.7	22.3
Q0351-390	03:53:19.20	-38:55:56.0	3.007	0.010	714	NC	091223	600	0.7	23.9
CTS0246	04:04:01.90	-33:35:00.0	3.042	0.007	521	NC	091223	800	0.7	20.4
CTQ0247	04:07:18.00	-44:10:14.0	3.021	0.010	714	NC	091223	1000	0.7	25.6
CTS0648	04:39:06.90	-50:47:40.0	2.947	0.007	521	NC	091222	1200	0.7	21.5
CTS0260	04:45:52.00	-31:58:43.0	2.722	0.006	521	NC	091222	900	0.7	22.0
H0449-1325	04:51:42.60	-13:20:33.0	3.107	0.007	521	NC	091222	1100	0.7	23.6
CTS0269	05:17:42.20	-37:54:46.0	3.045	0.007	521	NC	091222	800	0.7	21.7
Q0642-506	06:43:27.00	-50:41:13.0	3.107	0.007	521	NC	091222	900	0.7	19.9
GB6J0833+1123	08:33:14.36	+11:23:36.3	2.986	0.007	521	NC	091222/23,110329	3600	0.7	33.2
SDSSJ0904+1309	09:04:23.37	+13:09:20.7	2.975	0.007	521	NC	091222/23	1800	0.7	38.1
HE0940-1050	09:42:53.40	-11:04:25.0	3.076	0.007	521	NC	091222	800	0.7	36.5
CTS0281	09:52:33.30	-23:53:48.0	2.904	0.008	631	NC	091222,110329	2400	0.7	28.8
PKS1010-427	10:12:37.80	-42:58:37.8	2.962	0.007	521	NC	091223	1000	0.7	16.6
TXS1033+137	10:36:26.88	+13:26:51.7	3.098	0.007	521	NC	110328	1200	0.7	19.9
CTS0296	10:58:09.20	-26:05:39.0	2.887	0.007	521	NC	091222	900	0.7	29.8
HS1200+1539	12:03:31.29	+15:22:54.7	2.985	0.007	521	NC	110328,120711	2100	0.7	41.9
LBQS1209+1524	12:12:32.04	+15:07:25.6	3.067	0.007	521	NC	110329	2400	0.7	21.1
Q1210-1049	12:12:52.10	-11:06:10.0	2.938	0.007	521	NC	120712	2700	0.7	17.0
LBQS1223+1753	12:26:07.19	+17:36:49.8	2.953	0.009	654	NC	110329	1200	0.7	23.4
SDSSJ1241+1230	12:41:58.18	+12:30:59.3	2.979	0.009	714	NC	120711	3600	0.7	12.3
CTS0320	13:17:44.10	-31:47:14.0	2.965	0.007	521	NC	110328	2200	0.7	19.7
LBQS1345-0120	13:48:16.65	-01:35:09.9	2.957	0.007	521	NC	120713	2700	0.7	26.0
CTS0331	14:01:38.00	-13:46:10.0	3.022	0.011	792	NC	120715	2700	0.7	20.4
Q1406+123	14:08:38.92	+12:07:09.6	2.944	0.007	521	NC	120714	3000	0.7	33.2
Q1455+123	14:58:07.50	+12:09:37.8	3.057	0.007	521	NC	120712	3000	0.7	18.6
Q1508+087	15:10:47.37	+08:35:35.2	2.999	0.011	792	NC	120713	3300	0.7	13.1
Q1510+105	15:13:04.41	+10:23:30.8	3.064	0.007	521	NC	120715	3600	0.7	23.0
SDSSJ1559+1631	15:59:36.89	+16:31:01.5	3.072	0.009	631	NC	120715	3600	0.7	18.0
SDSSJ1604+1645	16:04:41.47	+16:45:38.3	2.888	0.010	792	NC-B	100813	2900	0.7	56.7
Q1623+155	16:25:47.21	+15:27:21.1	3.060	0.009	631	NC	120712	2700	0.7	14.3
PMNJ1837-5848	18:37:53.80	-58:48:09.0	3.041	0.007	521	NC	120712/15	5700	0.7	6.2
Q2117-4600	21:21:11.50	-45:47:58.0	2.957	0.007	521	NC	120715	3600	0.7	8.9
Q2119-4307A	21:22:28.70	-42:54:38.0	2.952	0.007	521	NC-B	120713	3600	0.7	16.4
Q2135-1335	21:27:45.40	-13:22:13.0	2.928	0.007	521	NC	100813/14	2700	0.7	21.5
FBQS2129+0037	21:29:16.60	+00:37:56.6	2.961	0.007	521	NC	100814	1100	0.7	26.3
CTS0358	21:41:44.40	-38:40:41.0	3.102	0.009	631	NC	120715	3300	0.7	22.0
PSGS2144+0542	21:47:22.26	+05:56:19.5	2.909	0.007	521	NC	120715	3600	0.7	12.2
SDSSJ2201+1256	22:01:16.75	+12:56:36.4	2.927	0.009	714	NC	120713	3000	0.7	17.5
FBQSJ2207+0101	22:07:08.32	+01:01:25.2	2.904	0.007	521	NC	120715	3000	0.7	26.2
PC2211+0119	22:14:27.80	+01:34:57.0	3.109	0.007	521	NC	120713	3000	0.7	20.6
LBQS2231-0015	22:34:08.99	+00:00:01.6	3.025	0.010	714	NC	100813	1200	0.7	31.3
HE2243-6031	22:47:09.10	-60:15:45.0	3.005	0.011	792	NC	100813,120712	1500	0.7	56.1
UM659	23:14:07.20	-03:25:28.0	3.056	0.009	631	NC	120712	2700	0.7	14.6
PKS2314-340	23:16:43.39	-33:49:12.5	2.963	0.007	521	NC-B	100813	1200	0.7	24.2
FBQS2330-0120	23:30:54.40	-01:20:53.0	2.910	0.007	521	NC	100814	1500	0.7	14.0
FBQSJ2339+0030	23:39:30.00	+00:30:17.3	3.053	0.007	521	NC	120712	2700	0.7	20.1
UM184	23:50:57.87	-00:52:09.9	3.021	0.010	714	NC	120712	3000	0.7	23.8
SDSSJ0010-0037	00:10:22.17	-00:37:01.3	3.153	0.007	521	C	100814	1200	0.7	12.3
SDSSJ0043-0015	00:43:23.43	-00:15:52.6	2.829	0.008	631	C	100814	1200	0.7	18.6
SDSSJ0125-1027	01:25:30.85	-10:27:39.8	3.356	0.008	521	C	100813/14	2400	0.7	27.8
SDSSJ0139-0824	01:39:01.40	-08:24:43.9	3.016	0.010	714	C	091223,100813/14	3600	0.7	21.0
SDSSJ0145-0945	01:45:16.59	-09:45:17.3	2.732	0.006	521	C	100813	900	0.7	37.0
SDSSJ0145-0945B	01:45:16.76	-09:45:17.9	2.731	0.006	521	C	100813	1500	0.7	14.9
SDSSJ0148-0907	01:48:50.64	-09:07:12.8	3.322	0.008	521	C	100814	1200	0.7	22.4
SDSSJ0209-0005	02:09:50.70	-00:05:06.4	2.858	0.007	521	C	100814	900	0.7	37.2
SDSSJ0251-0737	02:51:51.20	-07:37:07.7	3.084	0.007	521	C	091223	1000	0.7	12.9
SDSSJ0303-0023	03:03:41.04	-00:23:21.8	3.229	0.007	521	C	091223	900	0.7	24.4
SDSSJ0304-0008	03:04:49.86	-00:08:13.4	3.297	0.009	631	C	091223,100814	2000	0.7	34.0
SDSSJ0338-0005	03:38:54.77	-00:05:20.9	3.053	0.010	714	C	091223	1000	0.7	15.7
SDSSJ0859+0205	08:59:59.15	+02:05:19.7	2.979	0.009	654	C	091222/23	2400	0.7	27.9

Table 1 — *Continued*

Name	R.A. (J2000)	Dec. (J2000)	$z_{\text{qso}}$	$\sigma_{z,\text{qso}}^{\text{a}}$	$\sigma_{v,\text{qso}}^{\text{b}}$ (km s $^{-1}$ )	Notes $^{\text{c}}$	Date (yymmdd)	Exposure (sec)	Slit (")	S/N at 5500Å
SDSSJ0908+0658	09:08:32.28	+06:58:53.8	3.062	0.007	521	C	110329	1200	0.7	14.5
SDSSJ0915+0549	09:15:46.68	+05:49:42.7	2.976	0.007	521	C	110329	1200	0.7	23.7
SDSSJ0931-0000	09:31:53.12	-00:00:51.0	3.209	0.007	521	C	091223	1100	0.7	16.7
SDSSJ0937+0417	09:37:15.38	+04:17:37.6	3.127	0.007	521	C	091223	1100	0.7	16.6
SDSSJ0942+0422	09:42:02.04	+04:22:44.6	3.283	0.009	631	C	091222/23	1500	0.7	40.1
SDSSJ0947+1421	09:47:34.20	+14:21:17.0	3.041	0.007	521	C	110328	900	0.7	28.3
SDSSJ1004+0018	10:04:28.43	+00:18:25.6	3.050	0.009	631	C	091222/23	2100	0.7	24.9
SDSSJ1015+1118	10:15:39.35	+11:18:15.9	2.913	0.007	521	C	110329	1200	0.7	18.7
SDSSJ1019+0825	10:19:54.53	+08:25:15.0	2.989	0.007	521	C	110328	1200	0.7	23.7
SDSSJ1025+0452	10:25:09.64	+04:52:46.7	3.243	0.007	521	C	091223	900	0.7	20.2
SDSSJ1205-0048	12:05:32.23	-00:48:48.2	2.986	0.007	521	C	110328	1200	0.7	17.8
SDSSJ1405+0507	14:05:21.67	+05:07:44.4	2.994	0.007	521	C-B	110329	1200	0.7	18.0
SDSSJ1432+1139	14:32:12.86	+11:39:53.1	3.006	0.010	714	C-B	110329	1000	0.7	13.8
SDSSJ1459+0024	14:59:07.18	+00:24:01.2	3.024	0.007	521	C	110329	1500	0.7	16.6
SDSSJ1513+0855	15:13:52.52	+08:55:55.7	2.891	0.007	521	C	100812/13	2100	0.7	29.3
SDSSJ1521-0048	15:21:19.68	-00:48:18.6	2.949	0.007	521	C	100812	630	0.7	10.4
SDSSJ1550+0537	15:50:36.80	+05:37:49.9	3.153	0.009	631	C	100814	1100	0.7	21.3
SDSSJ1551+0908	15:51:03.39	+09:08:49.2	2.755	0.007	521	C	100814	1100	0.7	24.6
SDSSJ1608+0715	16:08:43.90	+07:15:08.6	2.888	0.008	631	C	100814	900	0.7	37.9
SDSSJ1615+0608	16:15:45.95	+06:08:52.4	3.062	0.007	521	C-B	110328	1200	0.7	18.6
SDSSJ1620+0941	16:20:50.27	+09:41:35.2	3.061	0.007	521	C	100814	1200	0.7	14.1
SDSSJ2038-0025	20:38:14.55	-00:25:38.9	2.707	0.006	521	C	100813/14	2700	0.7	23.2
SDSSJ2049-0554	20:49:46.35	-05:54:53.4	3.195	0.007	521	C	100813	1200	0.7	17.8
SDSSJ2055-0511	20:55:16.84	-05:11:11.0	3.004	0.010	714	C-B	100813/14	2400	0.7	27.6
SDSSJ2100-0641	21:00:25.03	-06:41:46.0	3.130	0.007	521	C	100814	1200	0.7	17.8
SDSSJ2222-0946	22:22:56.11	-09:46:36.2	2.914	0.007	521	C	100813	1200	0.7	22.8
SDSSJ2225-0041	22:25:59.52	-00:41:57.5	2.774	0.007	521	C	100814	1100	0.7	22.2
SDSSJ2238-0921	22:38:19.76	-09:21:06.0	3.278	0.007	521	C	100813	1200	0.7	20.9
SDSSJ2319-1040	23:19:34.77	-10:40:36.9	3.180	0.007	521	C	100813	1200	0.7	17.5
SDSSJ2334-0908	23:34:46.40	-09:08:12.3	3.351	0.008	521	C	100813	1200	0.7	24.0
SDSSJ2348-1041	23:48:56.48	-10:41:31.2	3.153	0.007	521	C	100813	1200	0.7	20.9

<sup>a</sup> Statistical error on the quasar redshift from broad emission lines.

<sup>b</sup> Corresponding error on the quasar redshift in velocity.

<sup>c</sup> C: color selected; NC: non color selected; B: broad absorption line quasar (visually classified)

**Table 2**  
Results of the  $\tau \geq 2$  LLS survey.

Name	Notes $^{\text{a}}$	$z_{\text{qso}}$	$z_{\text{start}}$	$z_{\text{end}}$	$z_{\text{lls}}$
FBQSJ0002+0021	NC	3.072	3.0315	2.5000	0.0000
Q0038-4041	NC	2.977	2.9374	2.8161	2.8161
LBQS0041-2638	NC	3.058	3.0176	2.5000	0.0000
LBQS0047-3050	NC	2.967	2.9275	2.5000	0.0000
UM669	NC-(1)	3.041	3.0008	2.9271	2.9271
Q0130-403	NC	3.031	2.9909	2.5620	2.5620
UM148	NC-(1)	3.001	2.9612	2.5000	0.0000
CTS0418	NC	2.916	2.8770	2.5828	2.5828
H0216+0803	NC-(1)	3.001	2.9612	2.5000	0.0000
CTS0220	NC	3.109	3.0681	2.7391	2.7391
Q0244-302	NC	3.088	3.0473	3.0473	3.0909
CTS0424	NC	3.036	2.9958	2.5738	2.5738
CTS0238	NC	3.112	3.0711	2.5000	0.0000
Q0351-3740	NC	2.952	2.9127	2.5000	0.0000
Q0351-390	NC-(2)	3.007	2.9671	2.5040	2.5040
CTS0246	NC	3.042	3.0018	2.5000	0.0000
CTQ0247	NC	3.021	2.9810	2.6219	2.6219
CTS0648	NC	2.947	2.9077	2.7957	2.7957
CTS0260	NC	2.722	2.6849	2.5000	0.0000
H0449-1325	NC	3.107	3.0661	2.9978	2.9978
CTS0269	NC	3.045	3.0047	2.5000	0.0000
Q0642-506	NC	3.107	3.0661	2.6591	2.6591
GB6J0833+1123	NC-(1)	2.986	2.9463	2.5000	0.0000
SDSSJ0904+1309	NC	2.975	2.9354	2.7690	2.7690
HE0940-1050	NC	3.076	3.0354	2.9169	2.9169
CTS0281	NC	2.904	2.8651	2.4968	2.4968
PKS1010-427	NC	2.962	2.9226	2.5000	0.0000
TXS1033+137	NC	3.098	3.0572	2.5977	2.5977
CTS0296	NC	2.887	2.8483	2.5432	2.5432
HS1200+1539	NC	2.985	2.9453	2.7077	2.7077
LBQS1209+1524	NC	3.067	3.0265	2.5000	0.0000
Q1210-1049	NC	2.938	2.8988	2.5000	0.0000
LBQS1223+1753	NC	2.953	2.9136	2.9136	2.9584



**Table 2** — *Continued*

Name	Notes <sup>a</sup>	$z_{\text{qso}}$	$z_{\text{start}}$	$z_{\text{end}}$	$z_{\text{lls}}$
SDSSJ1241+1230	NC	2.979	2.9394	2.9394	2.9870
CTS0320	NC	2.965	2.9255	2.5000	0.0000
LBQS1345-0120	NC	2.957	2.9176	2.8827	2.8827
CTS0331	NC	3.022	2.9820	2.5000	0.0000
Q1406+123	NC	2.944	2.9047	2.5000	0.0000
Q1455+123	NC	3.057	3.0166	2.6479	2.6479
Q1508+087	NC	2.999	2.9592	2.7222	2.7222
Q1510+105	NC	3.064	3.0235	2.8391	2.8391
SDSSJ1559+1631	NC	3.072	3.0315	3.0315	3.0611
SDSSJ1604+1645	NC-B	2.888	2.8493	2.5000	0.0000
Q1623+155	NC	3.060	3.0196	2.5000	0.0000
PMNJ1837-5848	NC	3.041	3.0008	2.7290	2.7290
Q2117-4600	NC	2.957	2.9176	2.5000	0.0000
Q2119-4307A	NC-B	2.952	2.9127	2.5362	2.5362
Q2135-1335	NC	2.928	2.8889	2.5000	0.0000
FBQS2129+0037	NC	2.961	2.9216	2.9173	2.9173
CTS0358	NC	3.102	3.0612	2.8932	2.8932
PSGS2144+0542	NC	2.909	2.8701	2.5000	0.0000
SDSSJ2201+1256	NC	2.927	2.8879	2.5000	0.0000
FBQSJ2207+0101	NC	2.904	2.8651	2.8651	2.8684
PC2211+0119	NC	3.109	3.0681	2.5000	0.0000
LBQS2231-0015	NC	3.025	2.9849	2.6525	2.6525
HE2243-6031	NC	3.005	2.9651	2.5000	0.0000
UM659	NC-(1)	3.056	3.0156	2.5000	0.0000
PKS2314-340	NC-B	2.963	2.9235	2.5000	0.0000
FBQS2330-0120	NC	2.910	2.8711	2.5000	0.0000
FBQSJ2339+0030	NC	3.053	3.0126	2.5000	0.0000
UM184	NC-(1)	3.021	2.9810	2.9295	2.9295
SDSSJ0010-0037	C	3.153	3.1117	3.1117	3.1166
SDSSJ0043-0015	C	2.829	2.7909	2.5000	0.0000
SDSSJ0125-1027	C	3.356	3.3126	2.5625	2.5625
SDSSJ0139-0824	C	3.016	2.9760	2.6776	2.6776
SDSSJ0145-0945	C	2.732	2.6948	2.5000	0.0000
SDSSJ0145-0945B	C	2.731	2.6939	2.5000	0.0000
SDSSJ0148-0907	C	3.322	3.2790	2.9949	2.9949
SDSSJ0209-0005	C-(1)	2.858	2.8196	2.5230	2.5230
SDSSJ0251-0737	C	3.084	3.0433	2.5000	0.0000
SDSSJ0303-0023	C-(1)	3.229	3.1869	2.9405	2.9405
SDSSJ0304-0008	C-(1)	3.297	3.2542	2.5354	2.5354
SDSSJ0338-0005	C	3.053	3.0126	2.7460	2.7460
SDSSJ0859+0205	C	2.979	2.9394	2.8455	2.8455
SDSSJ0908+0658	C	3.062	3.0216	2.5000	0.0000
SDSSJ0915+0549	C	2.976	2.9364	2.6632	2.6632
SDSSJ0931-0000	C	3.209	3.1671	2.9265	2.9265
SDSSJ0937+0417	C	3.127	3.0859	2.5000	0.0000
SDSSJ0942+0422	C	3.283	3.2404	2.4706	2.4706
SDSSJ0947+1421	C	3.041	3.0008	2.5000	0.0000
SDSSJ1004+0018	C	3.050	3.0097	2.7460	2.7460
SDSSJ1015+1118	C	2.913	2.8740	2.8700	2.8700
SDSSJ1019+0825	C	2.989	2.9493	2.9493	2.9647
SDSSJ1025+0452	C	3.243	3.2008	3.1296	3.1296
SDSSJ1205-0048	C	2.986	2.9463	2.5000	0.0000
SDSSJ1405+0507	C-B	2.994	2.9542	2.5000	0.0000
SDSSJ1432+1139	C-B	3.006	2.9661	2.5000	0.0000
SDSSJ1459+0024	C	3.024	2.9839	2.7675	2.7675
SDSSJ1513+0855	C	2.891	2.8523	2.5000	0.0000
SDSSJ1521-0048	C	2.949	2.9097	2.5000	0.0000
SDSSJ1550+0537	C	3.153	3.1117	2.9798	2.9798
SDSSJ1551+0908	C	2.755	2.7176	2.6997	2.6997
SDSSJ1608+0715	C	2.888	2.8493	2.5000	0.0000
SDSSJ1615+0608	C-B	3.062	3.0216	2.9882	2.9882
SDSSJ1620+0941	C	3.061	3.0206	2.8236	2.8236
SDSSJ2038-0025	C	2.707	2.6701	2.4896	2.4896
SDSSJ2049-0554	C	3.195	3.1532	2.5000	0.0000
SDSSJ2055-0511	C-B	3.004	2.9641	2.5000	0.0000
SDSSJ2100-0641	C	3.130	3.0889	3.0889	3.0913
SDSSJ2222-0946	C	2.914	2.8750	2.5000	0.0000
SDSSJ2225-0041	C	2.774	2.7364	2.5575	2.5575
SDSSJ2238-0921	C	3.278	3.2354	3.1280	3.1280
SDSSJ2319-1040	C	3.180	3.1384	2.6749	2.6749
SDSSJ2334-0908	C	3.351	3.3077	3.2260	3.2260
SDSSJ2348-1041	C	3.153	3.1117	2.9975	2.9975

<sup>a</sup> C: color selected; NC: non color selected; B: broad absorption line quasar (visually classified); (1): included in the survey by Sargent et al. (1989); (2): included in the survey by Lanzetta (1991).

**Table 3**  
Analysis of the metal lines in the LLS composite spectrum.

Ion	$\lambda_{\text{rest}}$ (Å)	$f$	$W^{\text{a}}$ (Å)	$\sigma_W$ (Å)	sign	$\log N_{\text{X,lin}}^{\text{a,c}}$ ( $\text{cm}^{-2}$ )	$\log N_{\text{X,aodm}}^{\text{a}}$ ( $\text{cm}^{-2}$ )	$\sigma_{\text{N,aodm}}$ ( $\text{cm}^{-2}$ )	Adopted Value
AlII	1670.7874	1.8800	0.039	0.010	=	11.93	11.94	0.12	$11.94 \pm 0.12$
AlIII	1854.7164	0.5390	0.096	-	<	12.77	12.78	-	< 12.78
AlIII	1862.7895	0.2680	0.076	-	<	12.97	12.97	-	
CII	1334.5323	0.1278	0.063	0.009	=	13.49	13.51	0.06	$13.51 \pm 0.06$
CIII <sup>b</sup>	977.0200	0.7620	0.655	0.067	>	14.01	14.24	0.09	> 14.24
CIV	1548.1950	0.1908	0.218	0.010	=	13.73	13.79	0.02	$13.81 \pm 0.04$
CIV	1550.7700	0.0952	0.127	0.009	=	13.80	13.82	0.03	
FeII	1608.4511	0.0580	0.047	-	<	13.55	13.56	-	< 13.56
OI	1302.1685	0.0489	0.121	-	<	14.22	14.24	-	< 14.24
SiII	1304.3702	0.0940	0.116	-	<	13.91	13.93	-	< 13.29
SiII	1526.7066	0.1270	0.050	-	<	13.28	13.29	-	
SiII	1808.0130	0.0022	0.084	-	<	15.12	15.13	-	
SiIII <sup>b</sup>	1206.5000	1.6600	0.524	0.085	>	13.39	13.57	0.10	> 13.57
SiIV	1393.7550	0.5280	0.156	0.008	=	13.24	13.27	0.02	$13.31 \pm 0.05$
SiIV	1402.7700	0.2620	0.095	0.010	=	13.32	13.34	0.05	
ZnII	2026.1360	0.4890	0.077	-	<	12.63	12.64	-	< 12.64

<sup>a</sup> For undetected transitions, we list the  $3\sigma$  upper limits.

<sup>b</sup> At MagE spectral resolution, this transition is likely to be saturated.

<sup>c</sup> The listed column densities are subject to significant uncertainties as discussed in the text.